frontiers in Earth Science

ORIGINAL RESEARCH
published: 24 March 2022
doi: 10.3389/feart.2022.825255

Multifrequency Spaceborne Synthetic Aperture Radar Data for Backscatter-Based Characterization of Land Use and Land Cover

Shatakshi Verma[1], *Shashi Kumar*[2]*, *Varun Narayan Mishra*[1] *and Rahul Raj*[3]

[1]Centre for Climate Change and Water Research, Suresh Gyan Vihar University, Jaipur, India, [2]Photogrammetry and Remote Sensing Department, Indian Institute of Remote Sensing (IIRS), ISRO, India, [3]Institute of Bio- and Geosciences, Agrosphere (IBG-3), Forschungszentrum, Jülich GmbH, Germany

Polarimetric synthetic aperture radar remote sensing extracts the information about the target using decomposition models to separate the polarimetric information into single-bounce (contributed by smooth surfaces), double-bounce (contributed by urban structure), and volume (mainly due to vegetation cover) scattering components. The penetration capacity of the electromagnetic wave into the surface increases with the decrease in its frequency. This study explores and compares the polarimetric decomposition models for scattering-based characterization of land use and cover using multifrequency spaceborne synthetic aperture radar sensor datasets that were acquired over San Francisco, CA, USA. The present work compares the scattering parameters of coherent (Pauli), roll-invariant (Barnes), eigenvalue–eigenvector (Cloude), and compact-polarimetric (Raney) decomposition modeling approaches for scattering-based characterization of urban structures, waterbody, and vegetation cover. The land use/cover classification was performed based on the scattering response of the scatterers using a support vector machine classifier. The outputs of the classification approach on multisensor, multifrequency, and multi-polarization polarimetric synthetic aperture radar data have shown reasonable accuracy in classifying the land use and land cover. The decomposition models fail to characterize the oriented urban structures that cause misclassification of urban structures as vegetation. The higher-order roll-invariant decomposition modeling approaches could improve the interpretation of different targets and accuracy in land use and land cover classification.

Keywords: multifrequency spaceborne SAR, eigenvalue-eigenvector, roll-invariant, compact-polarimetric decomposition, support vector machine, land use and land cover classification

OPEN ACCESS

Edited by:
Christian Bignami,
Istituto Nazionale di Geofisica e Vulcanologia (INGV), Italy

Reviewed by:
Milad Janalipour,
K. N. Toosi University of Technology, Iran
Mukesh Gupta,
Catholic University of Louvain, Belgium

***Correspondence:**
Shashi Kumar
shashi@iirs.gov.in

Specialty section:
This article was submitted to Environmental Informatics and Remote Sensing, a section of the journal Frontiers in Earth Science

Received: *30 November 2021*
Accepted: *14 February 2022*
Published: *24 March 2022*

Citation:
Verma S, Kumar S, Mishra VN and Raj R (2022) Multifrequency Spaceborne Synthetic Aperture Radar Data for Backscatter-Based Characterization of Land Use and Land Cover. Front. Earth Sci. 10:825255. doi: 10.3389/feart.2022.825255

INTRODUCTION

The development of polarimetric synthetic aperture radar (PolSAR) remote sensing has provided an opportunity to the scientific community and researchers to study the polarimetric properties of the objects on the Earth's surface (Schuler et al., 2003, Schuler et al., 2004; Sato et al., 2012; Chen and Sato, 2013; Chen et al., 2014a; Kumar et al., 2022). The PolSAR remote sensing is based on the concept of electromagnetic (EM) wave polarization. The polarization state of the EM wave is defined by the amplitude, orientation angle, ellipticity, and direction of the electric field vector. The PolSAR

sensor emits the EM wave to the ground target in a specific polarization state. The target absorbs some EM energy and reradiates the rest of the EM energy as a new EM wave in a different state of polarization to the sensor. This change in polarization state depends on the shape, size, orientation, and dielectric property of the target (Lee and Pottier, 2009). Therefore, the study of polarimetric properties is essential for the characterization of different targets such as waterbody, buildings, bridges, and forest structures present on the Earth's surface, as each scatter produces a unique scattering response due to the differences in their dielectric and structural properties.

The PolSAR sensor can measure the scattering response of different types of scatterers within a single SAR resolution cell. The PolSAR sensor transmits the EM signal to the ground target in horizontal and vertical polarization mode and receives the backscatter signal horizontally and vertically, thus, providing the information in four polarimetric channels HH, HV, VH, and VV. It has been found that the polarimetric distortions present in the PolSAR data also affect the scattering retrieval contributed by different scatterers (Babu et al., 2021a, Babu et al., 2021b; Maiti et al., 2021). However, this is not a problem in recent days because concerned space agencies provide the data free from the polarimetric distortions, so the user should not get difficulty in accurate scattering retrieval from SAR data (Kumar et al., 2022). The polarimetric responses are sensitive to the dielectric and structural property of the imaged ground target. This polarimetric information can be decomposed into different scattering components such as surface/odd, double-bounce/dihedral, and volume, which describes the scattering mechanisms of the ground target. The odd-bounce scattering response is given by the smooth surfaces or Bragg's scatterers such as waterbody, double-bounce scattering response is produced by the high-rise buildings, and the volume scattering response is generated by the vegetation structures. These scattering components are useful for the characterization of the target within a single SAR resolution cell. Therefore, the decomposition of the PolSAR dataset is essential to retrieve the scattering information. There are various PolSAR-based (Cloude, 1985; Holm and Barnes, 1988; Krogager, 1990; van Zyl, 1993; Freeman and Durden, 1998; Yamaguchi et al., 2005; Freeman, 2007) and PolSAR Interferometry (PolInSAR)-based (Chen et al., 2014b; Agrawal et al., 2016; Shafai and Kumar, 2020; Bhanu Prakash and Kumar, 2021a; Bhanu Prakash and Kumar, 2021b) decomposition modeling approaches for extracting the scattering components from PolSAR datasets to study the different scattering mechanisms of the targets.

The decomposition modeling approaches are categorized as "coherent" and "incoherent," "model-based" and "eigenvalue/eigenvector" based, and the decomposition based on the dichotomy of the "Kennaugh matrix (K)." The coherent target decomposition models provide suitable information about coherent targets or pure single targets. It is considered that a "pure target" produces the coherent scattering or complete polarized response free from any external noise caused by a cluttered environment or time variation of target exposure for the incident EM wave. The coherent decomposition models are used directly on the scattering matrix. In contrast, the incoherent target decomposition is favorable for studying "distributed targets." Generally, the dynamics of changing environment causes spatial and temporal variation to the imaging radar targets, leading to the concept of "distributed targets." It is considered that "distributed targets" produce a partially polarized scattering response. The incoherent decomposition models are used on second-order statistics, *i.e.*, coherency matrix or covariance matrix.

The PolSAR sensor operates in the microwave region of the EM spectrum ranging from 1 mm to 1 m. These long-wavelength microwaves easily penetrate dust, smoke, and water vapor, which enable earth observation in all-weather conditions. The development of active SAR sensors brings the additional advantage that allows continuous monitoring of the Earth's surface, *i.e.*, both day and night. There are different frequencies/wavelength bands used by the PolSAR sensor such as Ka—0.75–1.1 cm, K—1.1–1.67 cm, Ku—1.67–2.4 cm, X—2.4–3.8 cm, C—3.8–7.5 cm, S—7.5–15 cm, L—15–30 cm, and P—30–100 cm. Generally, the penetration capacity of the EM wave increases as the wavelength increases. Thus, each frequency band has their characteristic and applications. The longer wavelengths, such as L-band, can easily penetrate through the surface feature such as soil, ice, or forest canopy, which causes more interaction of emitted EM signal with the subsurface targets, branches, leaves, and tree trunks, and provide subsurface feature information. Therefore, the longer wavelengths are suitable for retrieval of subsurface information such as forest height estimation (Kumar et al., 2020), forest aboveground biomass retrieval (Kumar et al., 2019), mapping land subsidence (Ng et al., 2012; Chaussard et al., 2013), and archaeological studies (Stewart et al., 2013). The shorter wavelengths, such as X-band, have relatively less penetration capacity. The emitted EM wave interacts with the top layer of the soil, ice, or forest canopy and provides less subsurface information. Therefore, the shorter wavelengths are suitable for sea ice monitoring (Scheuchl et al., 2014), flood detection (Mason et al., 2010), oil spill observation (Velotto et al., 2011), and ship detection (Brusch et al., 2011).

In SAR remote sensing, the surface roughness is related to the wavelength used by the SAR sensor (λ), depression angle (Υ), and local height of the object (h). The "Rayleigh criteria" is used to determine the surface roughness in SAR imagery (Bole et al., 2014). The smooth surface acts as a specular reflector, most of the EM wave will backscatter away from the SAR sensor, and the SAR sensor will receive a very low backscatter signal. The rough surface acts as a diffuse reflector, the EM wave will be scattered in all directions, and the SAR sensor will receive a strong backscatter signal.

The scattering mechanism described by the radar target is greatly affected by its shape, size, and frequency or wavelength used by the SAR sensor (Ferro-Famil and Pottier, 2016). The scattering behavior of the target is determined by the ratio of the size of the target and the sensor's wavelength. Therefore, the

sensitivity to the surface roughness decreases with an increase in the wavelength. The high-frequency or shorter EM wave can easily scatter from the surface, causing diffuse reflection, and low-frequency or longer EM wave easily penetrates through the surface, causing dominant specular reflection. Thus, an irregular surface may appear smooth in L-band, and a similar surface may appear very rough in X-band.

Many space agencies have launched radar satellites for the polarimetric-based study of the Earth's surface and subsurface features. National Aeronautics and Space Administration (NASA) was a pioneer to launch the first-ever synthetic aperture radar satellite "SeaSAT" in 1978. The SeaSAT's SAR sensor provided L-band HH polarization (HH → horizontal transmit and vertical receive) datasets (Jordan, 1980). Canada's radar satellite RADARSAT-2 launched in 2008, the successor of RADARSAT-1 (operational period—1995–2013); the sensor acquires quad-polarization (HH, HV, VV, and VH) datasets in C-band (Mahmood, 1997; Morena and James, 2004; Ali et al., 2014). The Japan Aerospace Exploration Agency (JAXA) had a Phased Array L-band Synthetic Aperture Radar (PALSAR-1) instrument onboard the Advanced Land Observation Satellite (ALOS)-1 spacecraft (2006–11) successor to SAR Japanese Earth Resources Satellite (JERS), and the PALSAR-1 instrument collected quad-pol radar images in L-band; the next descendant ALOS-2/PALSAR-2 of ALOS mission was launched in 2014 to acquire high-resolution fully polarimetric dataset in L-band (Rosenqvist et al., 2007, Rosenqvist et al., 2014). The currently operational Gaofen-3 spacecraft, which was launched in 2016, China's first SAR satellite, operates in C-band and provides quad-polarization datasets (Zhao et al., 2021). The Indian space agency launched the first Radar Imaging Satellite (RISAT-1) in 2012 (Misra et al., 2013), which was supplementary to the Indian remote sensing satellite (IRS) class satellite. The sensor operated in hybrid polarimetric mode, *i.e.*, the sensor transmits circular polarization signal in the C band and receives either horizontal or vertical polarization signal. The polarimetric data of RISAT-1 have been widely used in different thematic applications (Babu et al., 2019a; Tomar et al., 2019; Awasthi et al., 2020; Chaudhary and Kumar, 2020). In 2007, Germany joined the sphere of SAR remote sensing with the launch of the TerraSAR-X spacecraft, and the sensor is capable of acquiring very high-resolution quad-polarization datasets in X-band (Werninghaus and Buckreuss, 2010). Recently, NASA–Indian Space Research Organisation (ISRO) jointly has developed NASA–ISRO SAR (NISAR) spacecraft, which is expected to be launched in 2023, which will provide the fully polarimetric dataset in L- and S-bands (Rosen et al., 2017).

The classification of polarimetric datasets has gained wide attention due to its ability to measure the polarimetric response of the ground features. These polarimetric signatures in various polarization bases give a more detailed insight into radar targets (Jafari et al., 2015; Buono et al., 2017). Also, the development of polarimetric decomposition models has intensified its application in land use/land cover (LULC) classification because it provides scattering information associated with the ground targets (Alberga, 2007; Saito et al., 2018; Yin et al., 2018). A comparative study was done by Lardeux et al. (2009) using different polarimetric indicators derived from the decomposition of PolSAR datasets. The result showed that the support vector machine (SVM) algorithm outperforms the conventional Wishart classification approach. Another novel effort was made by Qi et al. (2012) for LULC classification. The combination of polarimetric decomposition and polarimetric SAR interferometric parameters was used to retrieve the information of textural and spatial features. A decision tree classifier was used for the classification. Bai et al. (2021) showed the improvement of the classification approach based on the integration of optical and SAR data to extract the urban and vegetation land cover feature. Niu and Ban (2013) significantly improved the classification accuracy using the polarimetric parameter of decomposition models derived from the multi-temporal SAR dataset.

Over the last few years, various classification methods based on statistical and nonstatistical approaches have been used to classify the Earth observation datasets (Lu, 2007; Kumar et al., 2015; Mishra et al., 2017a). Scientists are exploiting the machine learning approach for image classification practices (Mishra et al., 2017a; Yin et al., 2018, 2020; Chaudhary and Kumar, 2021; Rawat et al., 2021; Garg et al., 2022) due to its ability to handle multiple datasets and shows good accuracy in the classification results than other conventional approaches. Advanced machine learning-based classification algorithms such as SVM, artificial neural network, decision tree, and random forest have been extensively used for the LULC classification of satellite images (Kumar et al., 2015; Mishra et al., 2017b). The SVM algorithm has received substantial attention because of several advantages over the traditional classification method. It is sensitive to the dimensionality of the data accompanied by the size of training datasets (Pal and Foody, 2010; Kumar et al., 2015). It does not assume a probability distribution of the training datasets; as a substitute, it finds a decision from the training data directly based on a kernel function in a suitable space. The potentiality of the SVM method has attracted a great deal and is reported in many studies (Kumar et al., 2015; Kranjčić et al., 2019; Mishra et al., 2019; Orieschnig et al., 2021).

The scattering response of the target depends on the frequency used by the SAR sensor. A surface may appear rough in X-band; the high-frequency EM wave will easily scatter from the surface, causing diffuse reflection; a similar surface may appear smooth in L-band, as the EM wave easily penetrates through the surface, causing specular reflection. Therefore, it is necessary to study the unique polarimetric scattering response of radar targets such as waterbody, vegetation, and urban structure in different frequency ranges using fully polarimetric SAR datasets. The prime focus of this study is to compare the polarimetric parameters of decomposition modeling approaches for scattering-based characterization of LULC using multifrequency spaceborne SAR sensor datasets. The objectives of this study are as follows:

- extraction of the scattering components from multifrequency polarimetric SAR datasets using coherent (Pauli), roll-invariant (Barnes), eigenvalue–eigenvector (Cloude), and compact-polarimetric (CP) (Raney) decomposition modeling approaches.

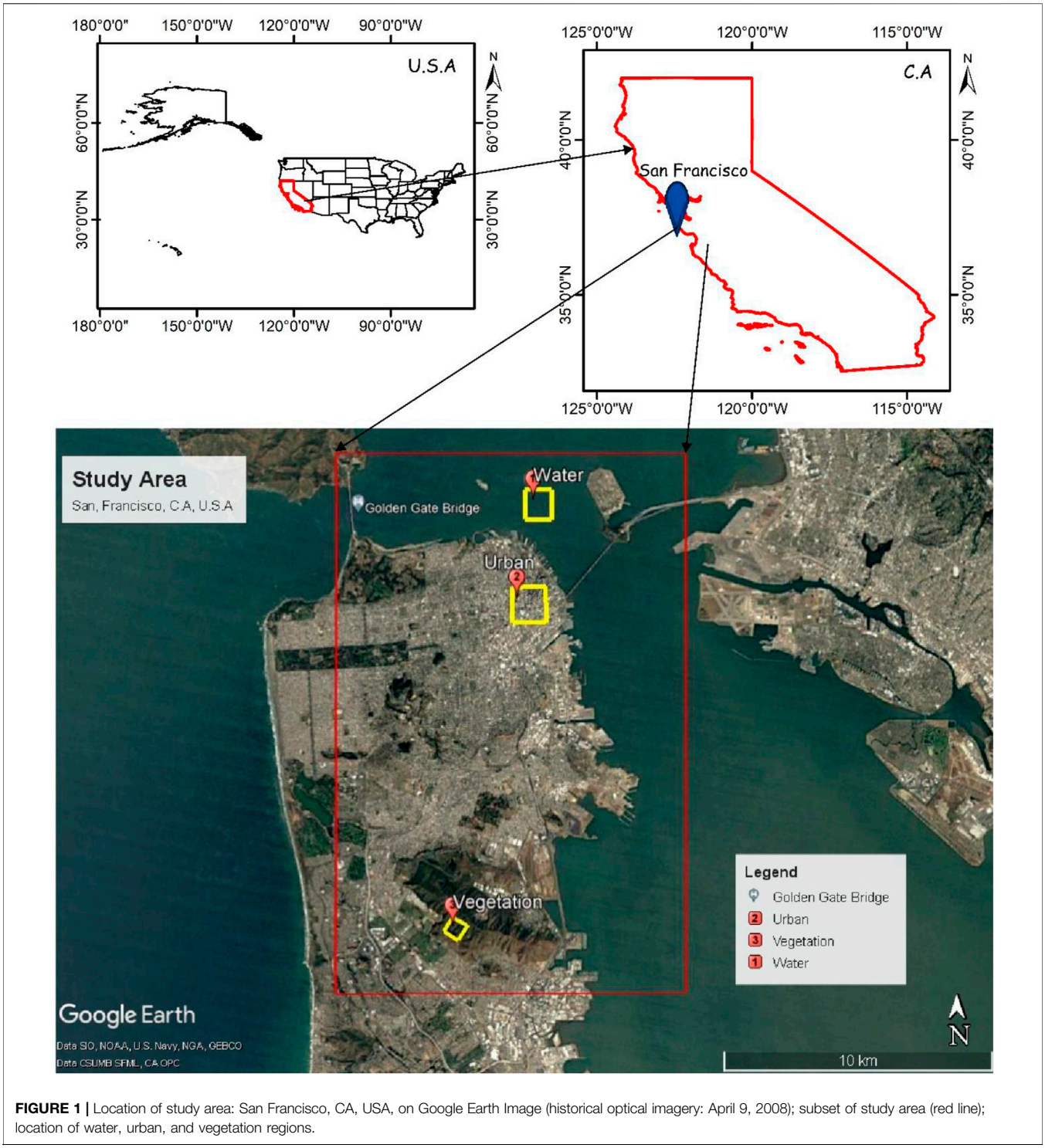

FIGURE 1 | Location of study area: San Francisco, CA, USA, on Google Earth Image (historical optical imagery: April 9, 2008); subset of study area (red line); location of water, urban, and vegetation regions.

- comparison of the scattering components of Pauli, Barnes, Cloude, and Raney decomposition models for characterization of the waterbody, urban, and vegetation structures.
- analysis of the accuracy of Pauli, Barnes, Cloude, and Raney scattering components for LULC classification using an SVM classifier.

STUDY AREA AND DATASETS

The study site is located on San Francisco Peninsula on the west coast of the United States. This area is enclosed by the San Francisco Bay, Pacific Ocean, and the Golden Gate strait (**Figure 1**). The study site consists of natural and artificial features such as vegetation, forests, parks, buildings, roads,

TABLE 1 | Description of datasets: SLC—single look complex; Quad-Pol—HH, HV, VH, and VV.

Satellite/Sensor	RADARSAT-2	ALOS-1 PALSAR-1	ALOS-2 PALSAR-2	TerraSAR-X	RISAT-1	Gaofen-3
Product ID	PDS_00,058,900	ALOS-P1_1__A-ORBIT__ALPSRP202350750	ALOS2-HBQR1_1_A-ORBIT_ALOS2044980750-150324	TSX1_SAR_SSC_BTX1_SM_Q_DRA_20151220T141542_20151220T141549	163,791,211	2,599,253
Product type	SLC	SLC	SLC	SLC	SLC	SLC
Date (mm-dd-yyyy) and time (hh-mm-ss) of acquisition	04–09-2008 02:01:39 (UTC)	11–11-2009 06:28:43 (UTC)	03–24-2015 08:01:55 (UTC)	12–20-2015 14:13:58 (UTC)	08–09-2016 02:03:45 (UTC)	09–15-2017 01:56: 41 (UTC)
Frequency (GHz), Wavelength (cm)	C-band 5.40 GHz 5.6 cm	L-band 1.26 GHz 23.8 cm	L-band 1.23 GHz 24.3 cm	X-band 9.64 GHz 3.1 m	C-band 5.35 GHz 5.6 m	C-band 5.40 GHz 5.6 cm
Polarization	Quad-Pol	Quad-Pol	Quad-Pol	Quad-Pol	Hybrid-Pol (RH, RV)	Quad-Pol
Incidence Angle	28.92°	23.87°	33.85°	39.69°	38.19°	21.22°
Pass	ASCENDING	ASCENDING	ASCENDING	DESCENDING	ASCENDING	ASCENDING
Range spacing × Azimuth spacing	4.73 × 4.82 m	9.36 × 3.54 m	2.86 × 3.20 m	2.31 × 2.31 m	1.80 × 2.33 m	5.36 × 2.24 m
No. of Scan lines and Samples	14,416, 2,823	18,432, 1,248	22,608, 8,080	10,673, 8,833	13,843, 8,719	7,173, 5,829
Multi-look Factors	1 × 2	1 × 7	1 × 2	5 × 8	4 × 5	1 × 7
No. of Rows and Column (subset)	1,674, 2049	654, 800	4,451, 4,896	7,006, 8,571	4,598, 5,625	2,102, 2,571

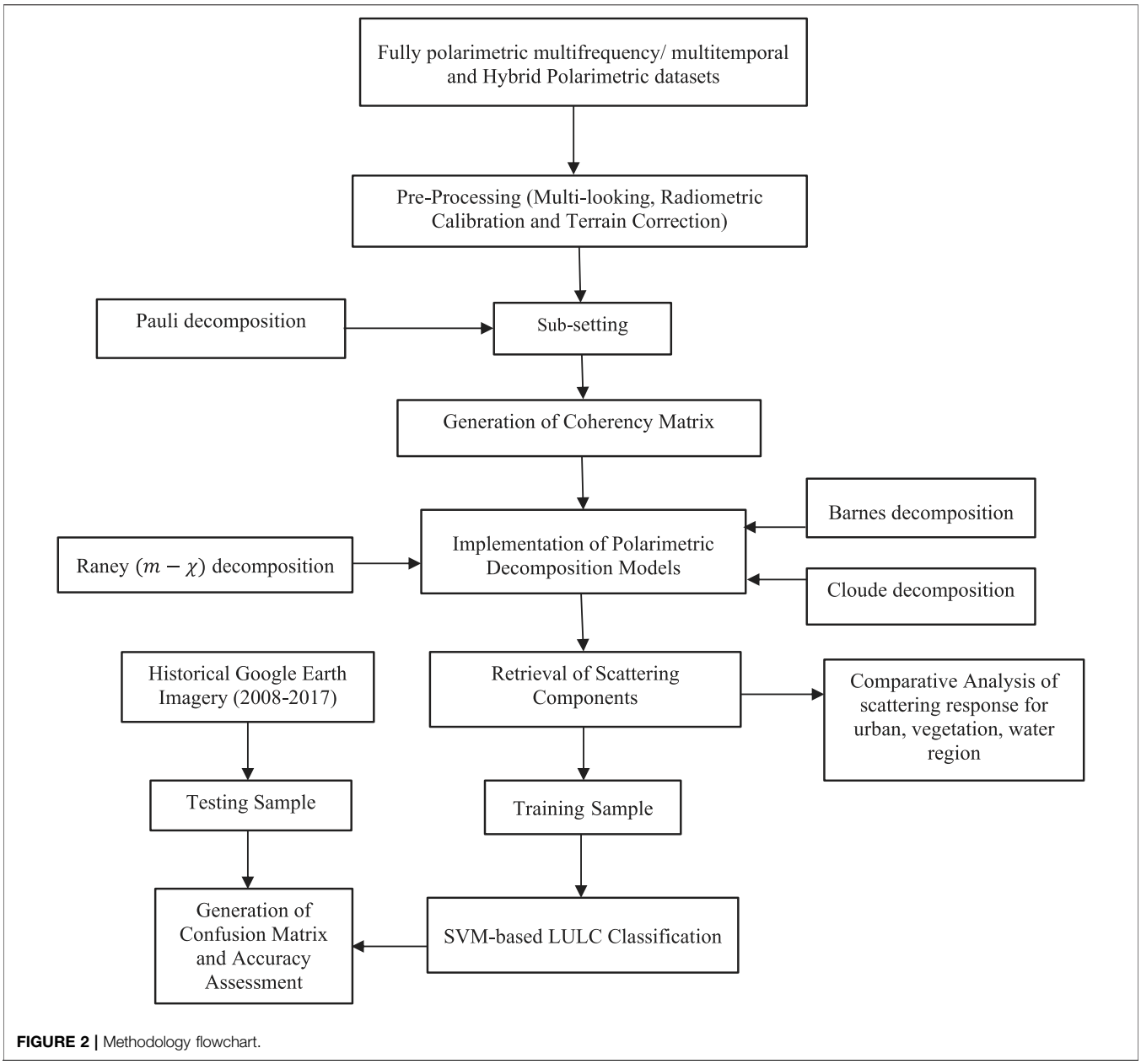

FIGURE 2 | Methodology flowchart.

hilly terrain, ponds, and sea surface. The urban features of the study area illustrate both orthogonal and oriented urban structures. The orthogonal urban structure refers to the building structure that is orthogonal to the imagery. The oriented urban structure refers to the building structure oriented at some angle to the imagery. Therefore, the diversity of different land features of the study area is suitable for this work.

The objective of this work is the comparison of polarimetric parameters for the scattering-based characterization of LULC using multifrequency PolSAR datasets. The fully polarimetric multifrequency SAR datasets of the study area (San Francisco, C.A, United States) were not available for the same date. Therefore, this study utilizes multifrequency and multi-temporal fully polarimetric spaceborne SAR sensor datasets of ALOS-1 PALSAR-1, ALOS-2 PALSAR-2, RADARSAT-2, RISAT-1, Gaofen-3, and TerraSAR-X that were acquired over San Francisco, C.A, United States. The detailed description of datasets is given in **Table 1**.

METHODOLOGY

The PolSAR datasets were in single look complex (SLC) file format. The SLC SAR pixel represents the associated ground target information in the form of complex numbers—real and imaginary. Firstly, preprocessing (multi-looking, radiometric calibration, and terrain correction) of the polarimetric dataset was performed, then the coherency matrix was generated for

polarimetric analysis. After that, scattering components were retrieved using Pauli, Barnes, and Cloude decomposition models on the coherency matrix elements derived from fully polarimetric datasets, and the $m-\chi$ decomposition model proposed by Raney et al. (2012) was used for the hybrid polarimetric RISAT-1 dataset. The scattering response was measured for vegetation, waterbody, and urban regions. Then, SVM-based LULC classification was performed on the scattering components. The accuracy assessment was done for the comparative evaluation of LULC images.

For this work, SNAP 8.0 software (SNAP 8.0 released—STEP, 2022) was used for the preprocessing of the polarimetric datasets; ArcGIS 10.5 software (ArcGIS Desktop Download and Documentation, 2022) was used for the geocoding: the coherency matrix generation. The polarimetric decomposition models were utilized using PolSARPro 6.0.3 software (PolSARpro v6.0 Toolbox Download—STEP, 2022). The accuracy assessment was performed using ENVI 5.3 software (ENVI, 2022). The ground reference data for the accuracy assessment were collected from Google Earth Pro version 7.3 (https://www.google.com/intl/en_in/earth/versions/#earth-pro). **Figure 2** shows the methodological flowchart.

Data Preprocessing

The fully polarimetric multifrequency datasets were in SLC file format. The complex values of four channels—HH, HV, VV, and VH—are represented in a scattering matrix [S] (**Eq. 1**). In contrast, the CP sensor of RISAT-1 transmits the EM signal in the right circular mode, receives linear coherent backscattering response, and produces CP RH and RV datasets (Misra and Kirankumar, 2014; Babu et al., 2019b). The circular that transmits and linearly receives (CTLR) RH and RV datasets are expressed as complex scattering matrix [S] (Cloude et al., 2012) as of **Eq. 2**.

$$[S] = \begin{bmatrix} S_{HH} & S_{HV} \\ S_{VH} & S_{VV} \end{bmatrix} \tag{1}$$

$$\begin{bmatrix} E_{RH} \\ E_{RV} \end{bmatrix} = \frac{1}{\sqrt{2}} \begin{bmatrix} S_{HH} & S_{HV} \\ S_{VH} & S_{VV} \end{bmatrix} \begin{bmatrix} 1 \\ -i \end{bmatrix} = \frac{1}{\sqrt{2}} \begin{bmatrix} S_{HH} - iS_{HV} \\ S_{VH} - iS_{VV} \end{bmatrix} \tag{2}$$

Here, $S_{HH} \rightarrow$ horizontal transmits and horizontally receives polarized EM wave, $S_{HV} \rightarrow$ horizontal transmits and vertically receives polarized EM wave, $S_{VH} \rightarrow$ vertical transmits and horizontally receives polarized EM wave, $S_{VV} \rightarrow$ vertical transmits and vertically receives polarized EM wave, $E_{RH} \rightarrow$ right-hand circular transmits and horizontally receives polarized EM wave, and $E_{RV} \rightarrow$ right-hand circular transmits and vertically receives polarized EM wave.

Because the datasets were in SLC file format consisting of slant-range ambiguity, the multi-looking was performed to generate the square pixels; the number of range-looks and azimuth-looks for each dataset is shown in **Table 1**. The multi-looking process also reduces the speckle noise from the SAR pixels. Then, radiometric calibration was done to remove the ambiguity from the SAR pixels that arise due to fluctuation in transmission and receiving of signal from the radar sensor or due to variation in satellite roll angle and the sensor records errors in the datasets. After that, terrain correction was performed on the radiometrically corrected datasets to eliminate the geometric distortions such as layover, foreshortening, and shadows, which generally occur due to variations in terrain surface height and tilt in SAR sensors position (Lillesand and Kiefer, 1979).

Polarimetric Synthetic Aperture Radar Coherency Matrix

In a subset of the study area comprising forest cover, vegetation, parks, and dense urban structures, the water surface was taken for further processing of the datasets (**Figure 1**). The details of the number of rows and columns used for the subset are shown in **Table 1**. A polarimetric coherency matrix was produced from the scattering matrix [S] (**Eq. 1**), which is based on the Pauli spin matrix. Considering the monostatic SAR system, the following **Eq. 3** represents the Pauli feature vector corresponding to the ground target:

$$k_p = \frac{1}{\sqrt{2}}[S_{HH} + S_{VV} \quad S_{HH} - S_{VV} \quad 2S_{HV})]^T \tag{3}$$

Here, $k_p \rightarrow$ Pauli feature vector, $T \rightarrow$ transpose. Considering the ergodicity (variation in space and time) of the environment, second-order statistics, *i.e.*, coherency matrix (**Eq. 4**), produced by multiplying the Pauli feature vector (k_p) with its trans-conjugate (k_p^+). A coherency matrix consists of nine elements that describe the target physical structure and dielectric properties.

$$T_{3\times3} = \frac{1}{2}\begin{bmatrix} \langle|S_{HH}+S_{VV}|^2\rangle & \langle(S_{HH}+S_{VV})(S_{HH}-S_{VV})^*\rangle & 2\langle(S_{HH}+S_{VV})S_{HV}^*\rangle \\ \langle(S_{HH}-S_{VV})(S_{HH}+S_{VV})^*\rangle & \langle|S_{HH}-S_{VV}|^2\rangle & 2\langle(S_{HH}-S_{VV})S_{HV}{}^*\rangle \\ 2\langle S_{HV}(S_{HH}+S_{VV})^*\rangle & 2\langle S_{HV}(S_{HH}-S_{VV})^*\rangle & 4\langle|S_{HV}|^2\rangle \end{bmatrix} \tag{4}$$

Here, $\langle\ \rangle \rightarrow$ ensemble average, $||\ \rightarrow$ modulo, $* \rightarrow$ complex conjugate.

For the case of a single look CP SAR sensor system (Cloude et al., 2012), the CTRL datasets RH and RV are expressed as complex scattering matrix [S] as in **Eq. 3**. The stokes vector (S) is required to analyze the CP dataset (Raney et al., 2012). The polarization state of the monochromatic EM wave (**Eq. 5**) can be represented by the stokes vector. It consists of four real numbers—S_1, S_2, S_3, and S_4,—known as stokes parameters.

$$E = E_x + E_y \tag{5}$$

Here, $E_x = a_1 exp\ j(\tau + \theta_\circ)$ and $E_y = a_2 exp\ j(\tau + \theta_\circ + \delta)$ are horizontal and vertical components of EM wave, respectively, $a_1 \rightarrow$ amplitude of E_x, $a_2 \rightarrow$ amplitude of E_y, $\tau \rightarrow$ oscillation of EM wave, $\theta_\circ \rightarrow$ an arbitrary phase reference, and $\delta \rightarrow$ relative phase difference between E_x and E_y components. The stokes parameters of a monochromatic EM wave are given as—$S_1 = a_1^2 + a_2^2$, $S_2 = a_1^2 + a_2^2$, $S_3 = 2a_1a_2\cos\delta$, and$S_4 = -2a_1a_2\sin\delta$. The CP sensor provides four information—horizontal, vertical, and complex cross-product of the real and imaginary parts of the horizontal and vertical components. Considering the mode of CP

sensor as the right-hand circular transmission, the stokes parameter is given as (**Eq. 6**):

$$S = \begin{bmatrix} S_1 \\ S_2 \\ S_3 \\ S_4 \end{bmatrix} = \begin{bmatrix} \langle |E_{RH}|^2 + |E_{RV}|^2 \rangle \\ \langle |E_{RH}|^2 - |E_{RV}|^2 \rangle \\ 2Re\langle E_{RH} E_{RV}^* \rangle \\ -2Im\langle E_{RH} E_{RV}^* \rangle \end{bmatrix} \tag{6}$$

Here, Re, $Im \rightarrow$ real and imaginary values. The stokes vector in the form of 2 × 2 coherency matrix is expressed as (**Eq. 7**):

$$C2 = \begin{bmatrix} \langle E_{RH} E_{RH}^* \rangle & \langle E_{RH} E_{RV}^* \rangle \\ \langle E_{RV} E_{RH}^* \rangle & \langle E_{RV} E_{RV}^* \rangle \end{bmatrix} = \frac{1}{2} \begin{bmatrix} S_1 + S_2 & S_3 + iS_4 \\ S_3 - iS_4 & S_1 - S_2 \end{bmatrix} \tag{7}$$

Polarimetric Decomposition Models

The polarimetric decomposition models aim to separate the PolSAR datasets into different scattering components. The decomposition models are broadly classified as coherent and incoherent. Pauli, Kroggager, Polar, and Cameron are the coherent decomposition models. The incoherent decomposition is classified as model-based and eigenvalue–eigenvector decompositions.

The model-baseddecomposition is based on fitting the physical scattering mechanism sub-models to the SAR observation to retrieve the scattering components (Freeman and Durden, 1998; Yamaguchi et al., 2005; Yamaguchi et al., 2006; Freeman, 2007; Bhattacharya et al., 2015). The scattering mechanism associated with the cloud of randomly oriented dipoles (such as forest canopy structure) is termed as volume scattering, the even-bounce or double-bounce response was produced by a pair of orthogonal surfaces with two different dielectric constants (such as building and bridges), the moderately rough or Bragg scatter describes the odd-bounce or surface scattering response, and the helix scattering response is associated to the "helix target." The helix targets do not assume reflection symmetry in backscattering response and produce left- or right-hand circular polarization response for incident radar signal. Recently, two additional scattering mechanism models have been introduced for the oriented-dipole and compound dipole structures (Singh and Yamaguchi, 2018).

Huynen, Holms-Barnes, and Yang decompositions are based on the Kennaugh matrix "K" (Lee and Pottier, 2009). Huynen (1978) was the pioneer in developing the target decomposition theorems using PolSAR datasets. He proposed "phenological theory" to derive the radar scatterer's structural and physical properties. This theory aimed to isolate the radar backscattering response into a single residue target [*i.e.*, the stationary or "pure target" (T_0)] and a residue component [*i.e.*, a "distributed target" (T_N)]. He defined nine roll-invariant parameters called "Huynen Parameter" such that the N-target was independent of the line sight between the SAR sensor and the radar target. The following **Eq. 8** illustrates the Huynen N-target T_N and pure target T_0. The coherency matrix T_3 expanded into the single pure target (T_0), which has five degrees of freedom, and a residue target (T_N), which has the remaining four degrees of freedom. Huynen parameters define the target's real physical property and are suitable for the general study of the targets.

$$T_3 = \begin{bmatrix} \langle 2A_0 \rangle & \langle C \rangle - i\langle D \rangle & \langle H \rangle + i\langle G \rangle \\ \langle C \rangle - j\langle D \rangle & \langle B_0 \rangle + \langle B \rangle & \langle E \rangle + i\langle F \rangle \\ \langle H \rangle - j\langle G \rangle & \langle E \rangle - i\langle F \rangle & \langle B_0 \rangle - \langle B \rangle \end{bmatrix} = T_0 + T_N \tag{8}$$

Here, $T_3 \rightarrow$ the average coherency matrix is described by nine parameters: $A_0 \rightarrow$ total scattering power contribution of regular, smooth, and convex parts of scatterer; $B_0 \rightarrow$ total scattering power contribution of irregular, rough, and nonconvex depolarizing parts of the target; $B_0 + B \rightarrow$ the total contribution of symmetrical or irregular depolarized power; $B_0 - B \rightarrow$ total contribution of nonsymmetrical depolarized power; $C \rightarrow$ total depolarized power of symmetrical target global shape (linear), $D \rightarrow$ total depolarized power of symmetrical target local shape (curvature); $E \rightarrow$ total depolarized power of nonsymmetrical target local twist (torsion); $F \rightarrow$ total depolarized power of nonsymmetrical target global twist (helicity); $G \rightarrow$ total depolarized power of coupling between the asymmetric and non-symmetric component of global target; and $H \rightarrow$ total depolarized power of coupling between the asymmetrical and nonsymmetrical components of the global target.

The decomposition models are based on the eigenvalue–eigenvector of 3 × 3 Hermitian coherency T_3 matrix known as eigenvalue–eigenvector decomposition models (Lee and Pottier, 2009; Chen et al., 2018). This approach is roll-invariant and considered a substitute for the Huynen target decomposition approach. The decomposition of the polarimetric coherency T_3 matrix is given as **Eq.9**:

$$T_3 = U_3 \sum\nolimits_3 U_3^{-1} \tag{9}$$

$$\sum\nolimits_3 = \begin{bmatrix} \lambda_1 & 0 & 0 \\ 0 & \lambda_2 & 0 \\ 0 & 0 & \lambda_3 \end{bmatrix} \tag{10}$$

$$U_3 = [u_1\, u_2\, u_3] \tag{11}$$

where $\sum_3 \rightarrow$ 3 × 3 diagonal matrix representing real eigenvalues of T_3, *i.e.*, $\lambda_1 \geq \lambda_2 \geq \lambda_3 \geq 0$ and $U_3 \rightarrow$ the unitary matrix representing three-unit orthogonal eigenvectors of T_3, *i.e.*, u_1, u_2, u_3. **Eqs. 9–11** combined the decomposition of T_3, which can be represented as the sum of three independent targets as **Eq. 12**:

$$T_3 = \sum_{i=1}^{3} \lambda_i u_i u_i^{*T} = T_{01} + T_{02} + T_{03} \tag{12}$$

Here, $T_{01}, T_{02}, T_{03} \rightarrow$ equivalent scattering matrix for a deterministic scattering mechanism is described by eigenvalue (λ_i), and the type of scattering mechanism is specified by eigenvector (u_i); $u_i^{*T} \rightarrow$ conjugate transpose of eigenvector u_i. The eigenvalues and eigenvector are essential parameters for this decomposition. Cloude (1985) was a pioneer in developing eigenvector-based decomposition.

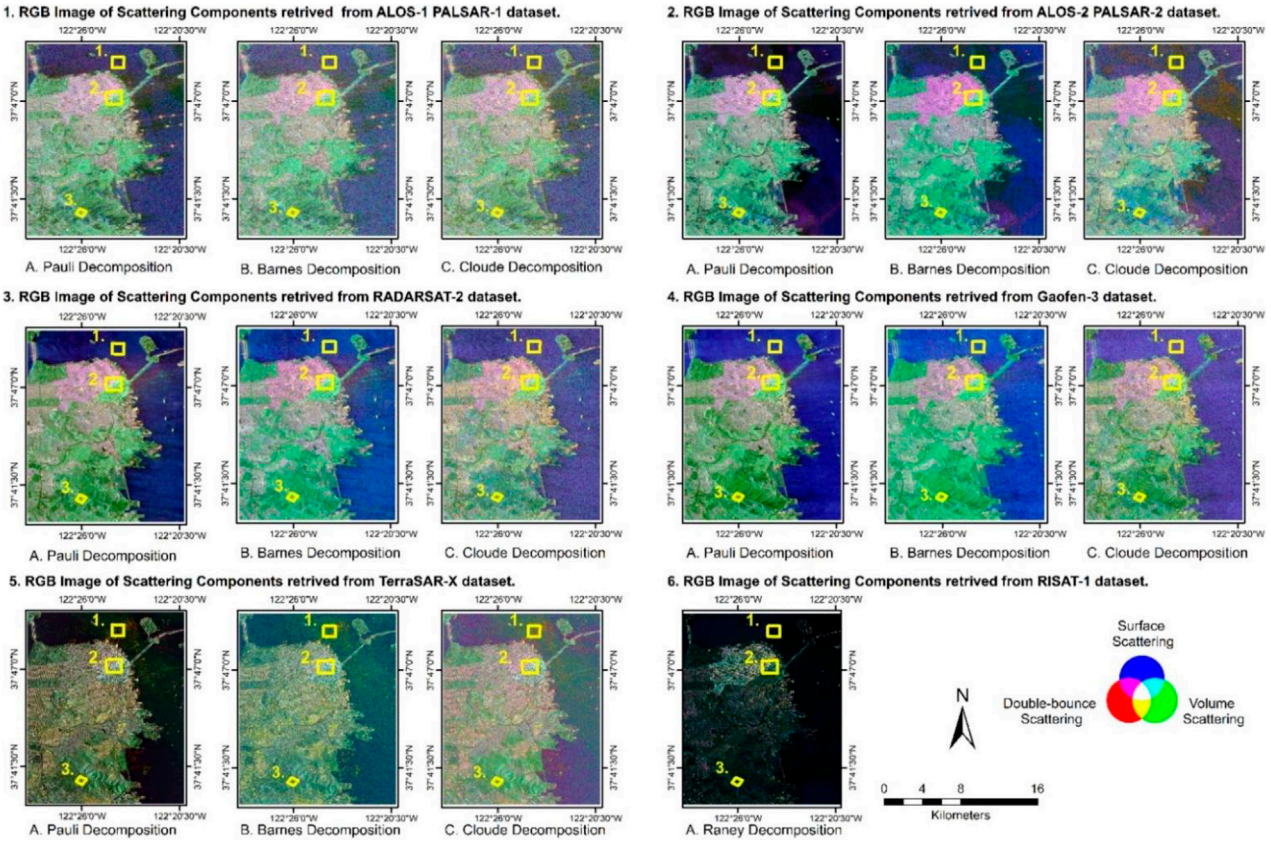

FIGURE 3 | Scattering components retrieved from multi-temporal and multifrequency SAR sensor ALOS-1 PALSAR-1, ALOS-2 PALSAR-2, RADARSAT-2, RISAT-1, Gaofen-3, and TerraSAR-X datasets. Color composite RGB image of (A) Pauli, (B) Barnes, (C) Cloude scattering components: red-double-bounce scattering, green-volume scattering, and blue-surface scattering; Location of (1) water, (2) urban, and (3) vegetation regions for analysis of scattering response.

The largest eigenvalue determines the dominant scattering mechanism. Similarly, van Zyl (1993) considered the eigenvalue of 3 × 3 covariance matrix for decomposition. They assumed a monostatic case for azimuthal symmetrical backscattering response from the natural terrain so that there exists no correlationbetween co-polar and cross-polar terms. They described four parameters—α,ρ,η,and μ —all depends on the shape, size, and electric and statistical angular distributions of the radar target. A hybrid approach was developed by Holm and Barnes (1988) for the decomposition based on the concept of eigenvalue/eigenvector and Huynen approach for the pure target (T_0) and distributed target (T_N). This decomposition represents the coherency matrix as the sum of three individual sub-matrices corresponding to the pure target, mixed target, and unpolarized mixed target, which is termed noise.

Pauli Decomposition

Pauli decomposition is coherent decomposition based on the Pauli spin matrix, as shown in **Eq. 13**. Here, the first element 1) corresponds to the odd bounce component associated with the smooth surface, the second elements 2) correspond to the double-bounce component associated with the corner reflectors such as walls and buildings, and the third 3) and fourth elements 4) correspond to the volume component associated with the forests or vegetations (Lee and Pottier, 2009).

$$S = \begin{bmatrix} S_{HH} & S_{HV} \\ S_{VH} & S_{VV} \end{bmatrix} = a/\sqrt{2}\begin{bmatrix} 1 & 0 \\ 0 & -1 \end{bmatrix} + b/\sqrt{2}\begin{bmatrix} 1 & 0 \\ 0 & -1 \end{bmatrix} + c/\sqrt{2}\begin{bmatrix} 0 & 1 \\ 1 & 0 \end{bmatrix} + d/\sqrt{2}\begin{bmatrix} 0 & -i \\ i & 0 \end{bmatrix} \quad (13)$$

where, $a = \frac{S_{HH}+S_{VV}}{\sqrt{2}}$, $b = \frac{S_{HH}-S_{VV}}{\sqrt{2}}$, $c = \frac{S_{HV}+S_{VH}}{\sqrt{2}}$, $d = \frac{S_{HV}-S_{VH}}{\sqrt{2}}$;

Considering the monostatic SAR system following the reciprocity principle, $S_{HV} = S_{VH}$, the fourth element becomes zero. *i.e.*, $d = 0$; hence, the remaining three elements, *i.e.*,a b, and c, describe the odd-bounce, even-bounce, and volume components, respectively.

The Pauli decomposition model was used on the scattering matrix [S] (**Eq. 1**), and $(S_{HH} + S_{VV})/\sqrt{2}$, $(S_{HH} - S_{VV})/\sqrt{2}$, and

$(S_{HV} + S_{VH})/\sqrt{2}$ as to 1) surface, 2) double-bounce, and 3) volume scattering components were retrieved, respectively. The RGB color composite image of the Pauli scattering components obtained from multifrequency PolSAR datasets is shown in **Figure 3**.

Barnes Decomposition

A roll-invariant decomposition technique was developed based on the Huynen N-target decomposition theorem (Lee and Pottier, 2009; Maghsoudi, 2011). Barnes objected to the theory of Huynen (1978), as the structural property derived from Huynen decomposition was not unique, and other decomposition techniques could present the same structural property. Hence, he proposed a generalized form of Huynen decomposition. The T_N (roll invariant parameter) was considered as vector space orthogonal to vector space T_0 (pure target). An arbitrary q vector belonging to N-target space was assumed so that $T_N q = 0$ and being roll invariant following **Eq. 14**,

$$T_N(\theta)q = 0 \rightarrow U(\theta)T_N U(\theta)^{-1}q = 0 \tag{14}$$

$$U(\theta)^{-1}q = \lambda q \tag{15}$$

Here, U $(\theta) \rightarrow 3 \times 3$ rotation matrix for angle "θ." The three eigenvectors $q1, q2$, and $q3$ are as follows:

$$q1 = \begin{bmatrix} 1 \\ 0 \\ 0 \end{bmatrix}; \; q2 = 1\Big/\sqrt{2}\begin{bmatrix} 0 \\ 1 \\ i \end{bmatrix}; q3 = 1\Big/\sqrt{2}\begin{bmatrix} 0 \\ i \\ 1 \end{bmatrix} \tag{15a}$$

Hence, the coherency matrix T_3 could be represented as pure target T_o and distributed target T_N in three ways:

- $q1 \rightarrow$ Huynen theorem decomposition
- $q2$ & $q3 \rightarrow$ Barnes theorem decomposition

The normalized target vectors k_{01}, k_{02}, and k_{03} corresponding to T_0 for $q1, q2$, and $q3$ are given by following **Eqs. 16–18**:

$$k_{01} = \frac{T_3 q_1}{\sqrt{q_1^{T*} T_3 q_1}} = \frac{1}{\sqrt{2\langle A_0 \rangle}}\begin{bmatrix} \langle 2A_0 \rangle \\ \langle C + jD \rangle \\ \langle H - jG \rangle \end{bmatrix} \tag{16}$$

$$k_{02} = \frac{T_3 q_2}{\sqrt{q_2^{T*} T_3 q_2}} = \frac{1}{\sqrt{2(\langle B_0 \rangle - \langle F \rangle)}}\begin{bmatrix} \langle C \rangle - \langle G \rangle + j\langle H \rangle - j\langle D \rangle \\ \langle B_0 \rangle + \langle B \rangle - \langle F \rangle + j\langle E \rangle \\ \langle E \rangle + j\langle B_0 \rangle - j\langle B \rangle - j\langle F \rangle \end{bmatrix} \tag{17}$$

$$k_{03} = \frac{T_3 q_3}{\sqrt{q_3^{T*} T_3 q_3}} = \frac{1}{\sqrt{2(\langle B_0 \rangle + \langle F \rangle)}}\begin{bmatrix} \langle H \rangle - \langle D \rangle + j\langle C \rangle - j\langle G \rangle \\ \langle E \rangle + j\langle B \rangle + j\langle B \rangle + j\langle F \rangle \\ \langle B_0 \rangle - \langle B \rangle + \langle F \rangle + j\langle E \rangle \end{bmatrix} \tag{18}$$

The Barnes decomposition model was used on the coherency matrix (**Eq. 4**) obtained in the previous step from fully polarimetric SAR datasets to retrieve the surface, double-bounce, and volume components. The RGB color composite image of the Barnes scattering components retrieved from multifrequency PolSAR datasets is shown in **Figure 3**.

Cloude Decomposition

Cloude (1985) made a significant approach for the retrieval of scattering elements based on the eigenvalue/eigenvector of the coherency matrix T_3, where the largest eigenvalue (λ_1) determines the dominant scattering mechanism of the coherency matrix T_3. Cloude et al. (Lee and Pottier, 2009) have formulated the target vector k_1 (**Eq. 20**) by considering the coherency matrix T_{01} as rank-1 and represented as a product of a single target vector k_1 as **Eq. 19**:

$$T_{01} = \lambda_1 u_1 \cdot u_1^{*T} = k_1 \cdot k_1^{*T} \tag{19}$$

$$k_1 = \sqrt{\lambda_1}u_1 = \frac{e^{i\phi}}{\sqrt{2A_0}}\begin{bmatrix} 2A_0 \\ C + iD \\ H - iG \end{bmatrix} = e^{i\phi}\begin{bmatrix} \sqrt{2A_0} \\ \sqrt{B_0 + B}\, e^{+i \arctan(D/C)} \\ \sqrt{B_0 - B}\, e^{-i \arctan(D/C)} \end{bmatrix} \tag{20}$$

Here, $\phi \in [-\pi, \pi] \rightarrow$ absolutephase ofthe target, $2A_0 \rightarrow$ surface scattering; $B_0 + B \rightarrow$ double-bounce scattering; $B_0 - B \rightarrow$ volume scattering. Cloude decomposition model was used on the coherency matrix (**Eq. 4**) to retrieve the scattering components. **Figure 3** shows the color-coded RGB image of Cloude scattering components retrieved from fully polarimetric multi-temporal and multifrequency datasets.

Raney Decomposition

Raney et al. (2012) proposed the $m - \chi$ decomposition for the CP SAR datasets. This decomposition approach requires two parameters, namely, degree of polarization m and degree of ellipticity χ. The chi (χ) is an essential parameter to describe the even *versus* odd backscattering signal. The degree of circularity of the polarizing ellipse is determined by utilizing the stokes parameter (**Eq. 21**).

$$\sin 2\chi = \left(\frac{-S_4}{mS_1}\right) \tag{21}$$

Raneydecomposition was used on the 2×2 coherency matrix elements (**Eq. 7**) retrieved from the CP dataset to extract the surface$\rightarrow$ $[mS_1(1 - \sin 2\chi)/2]^{1/2}$, double-bounce$\rightarrow$ $[mS_1(1 + \sin 2\chi)/2]^{1/2}$, and volume$\rightarrow$ $[S_1(1 - m)]^{1/2}$ components. **Figure 3** represents the color-coded RGB image of Raney scattering components obtained from CP RISAT-1 datasets.

Comparative Analysis of Scattering Response for Urban, Vegetation, and Water Surface

In this study, the mean pixel value of the surface, double-bounce, and volume scattering components derived from different decomposition modeling approaches were measured for the comparative study of scattering response for a waterbody, urban, and vegetation structure. **Figures 1** and **3** show the location of the test area on the optical image of Google Earth and the color-coded RGB image of scattering components, respectively. The present work utilizes multifrequency PolSAR

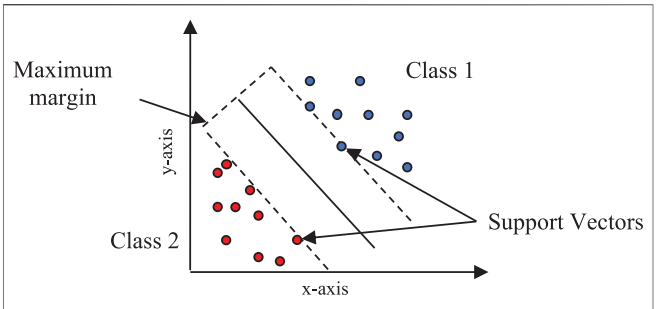

FIGURE 4 | Binary support vector machine.

datasets of different sensors which were acquired on different dates between the years 2008 and 2017. The historical optical images provided by Google Earth were used for validation. The historical optical images of Google Earth were coordinated to the date of acquisition of SAR imagery for the validation of the test area selected for urban, vegetation, and water regions; there was a very minor or negligible change in the testing area during the span of 9 years (2008–2017). The test area for the waterbody represents the smooth surface. Such targets describe surface scattering response because the emitted SAR signal interacts with a single dielectric surface. The chosen urban test region comprises both orthogonal and oriented urban. The urban structure is termed as corner reflectors or dihedral structures that produce a double-bounce scattering response due to the interaction of transmitted SAR signals with two different dielectric media. The scattering response was measured for both orthogonal and oriented urban structures. The selected vegetation test region comprises distributed vegetation structure over undulating terrain. The vegetation or forest canopy are complex structures that produce a volume scattering response due to the interaction of SAR signal with multiple dielectric media such as branches, leaves, and tree trunks.

Support Vector Machine-based Land Use/Land Cover Classification of Scattering Components.

SVM classifier is based on the statistical learning theory (Vapnik, 1995). This classifier requires small training samples and produces favorable results in the classification. Support vectors are the data points or training data closest to the hyperplane and affect the location of the hyperplane (decision boundary) in the space. In **Figure 4**, the SVM classifier creates a model based on the maximum margin hyperplane and divides the N-dimensional space into different classes (Boser et al., 1992; Vapnik, 1995; Chaudhary and Kumar, 2021).

The authors considered a case of binary SVM as in **Figure 4** (Chaudhary and Kumar, 2021). Suppose "$x_1, x_2, x_3, x_4 \ldots x_n$" be the training data that belongs to class 1 (red color dot) or class 2 (blue color dot), the decision function is expressed by (**Eq. 22**).

$$F(x) = w.x + b \tag{22}$$

where w = weight vector (orthogonal to hyperplane), and b = bias (parameter that maintains the position of hyperplane at the maximum margin). The position of the hyperplane is determined by **Eq. 23**.

$$w.x + b = 0 \tag{23}$$

The class of the data points is determined by the following: $w.x + b \geq 1 \rightarrow$ the data point falls above the hyperplane; $w.x + b \leq -1 \rightarrow$ the data point falls below the hyperplane. The SVM classifier was invented for binary structure classification (**Figure 4**). So, for the case of multi-class data, the SVM classifier creates multiple binary structures and determines the location of the hyperplane for each class based on the training data.

The SVM classifier was used for the LULC classification of the waterbody, urban, and vegetation using scattering components retrieved from different decomposition modeling approaches. The scattering response of the scatterers was used to train the SVM classifier. The radial bias function (RBF) was utilized for the classification. It requires less arithmetic calculative efforts and is capable of handling the nonlinear relationship between the input training pixels and the entire pixels of the datasets (Mishra et al., 2017a). The value of the RBF kernel is determined by the distance between the support vector point or the origin. **Equation 24** represents the RBF kernel used by the SVM classifier (Chaudhary and Kumar, 2021).

$$K_{RBF}(x_i, x') = \exp[-\gamma \|x_i - x'\|^2] \tag{24}$$

where $x_i - x^{'} \rightarrow$ Euclidian distance between training pixel data x_i and x' point data; $\gamma \rightarrow$ Gamma-the extent of kernel spread. The SVM classifier calculates the similarity index based on the distance between x_i training pixel data and x' point data. There are two tuning parameters to the RBF kernel, namely, penalty parameter "C- cost" and gamma (γ), which influence the overall accuracy of the classification. The penalty parameter "C" controls the degree of misclassification by imposing the rigid margin to adjust the trade-off between training sample data errors; hence, increasing its value creates a more accurate model. However, the large value of C may create over-fitting of the model (Qian et al., 2015). The gamma (γ) determines the potential of single data to affect the entire pixels of a dataset; it controls the shape of the hyperplane. For the classification of scattering components, the values of penalty parameters "C" and gamma (γ) were set to 100.00 and 0.33, respectively.

The study area is comprised of various LULC features: 1) land use urban features such as residential colonies, road networks, bridges, high-rise buildings, oriented buildings, and industrial area; 2) very few vegetation cover structures such as forest, vegetation, and urban green space; and 3) a small portion of water bodies such as swimming pools, ponds, and sea surface. To achieve better accuracy in the classification of vegetation, urban, and waterbody, the SVM classifier requires the training sample pixels to represent all the different types of features for each class. So, the training sample was collected for each type of feature representing

TABLE 2 | Description of training sample and testing sample used for SVM classification of surface (odd), double-bounce (dbl), and volume (vol) scattering components retrieved from decomposition models using multi-temporal and multifrequency datasets.

1	**Sensor/Satellite - ALOS 1 PALSAR 1, 11–11-2009**				
	Parameter	Class	Vegetation	Urban	Water
	Pauli scattering components (odd, dbl, vol)	Training Sample	223	582	246
		Testing Sample	111	289	121
	Barnes scattering components (odd, dbl, vol)	Training Sample	223	582	246
		Testing Sample	111	289	121
	Cloude scattering components (odd, dbl, vol)	Training Sample	223	582	246
		Testing Sample	111	289	121
2	**Sensor/Satellite- ALOS 2 PALSAR 2, 03-24—2015**				
	Parameter	Class	Vegetation	Urban	Water
	Pauli scattering components (odd, dbl, vol)	Training Sample	2,911	7,583	3,210
		Testing Sample	1,449	3,767	1,579
	Barnes scattering components (odd, dbl, vol)	Training Sample	2,911	7,583	3,210
		Testing Sample	1,449	3,767	1,579
	Cloude scattering components (odd, dbl, vol)	Training Sample	2,911	7,583	3,210
		Testing Sample	1,449	3,767	1,579
3	**Sensor/Satellite- RADARSAT 2, 04-09-2008**				
	Parameter	Class	Vegetation	Urban	Water
	Pauli scattering components (odd, dbl, vol)	Training Sample	1,261	3,287	1,391
		Testing Sample	628	1,633	684
	Barnes scattering components (odd, dbl, vol)	Training Sample	1,261	3,287	1,391
		Testing Sample	628	1,633	684
	Cloude scattering components (odd, dbl, vol)	Training Sample	1,261	3,287	1,391
		Testing Sample	628	1,633	684
4	**Sensor/Satellite- Gaofen-3, 09-15-2017**				
	Parameter	Class	Vegetation	Urban	Water
	Pauli scattering components (odd, dbl, vol)	Training Sample	1986	5,176	2,191
		Testing Sample	989	2,571	1,078
	Barnes scattering components (odd, dbl, vol)	Training Sample	1986	5,176	2,191
		Testing Sample	989	2,571	1,078
	Cloude scattering components (odd, dbl, vol)	Training Sample	1986	5,176	2,191
		Testing Sample	989	2,571	1,078
5	**Sensor/Satellite- TerraSAR-X, 12-20-2015**				
	Parameter	Class	Vegetation	Urban	Water
	Pauli scattering components (odd, dbl, vol)	Training Sample	5,672	14,825	6,278
		Testing Sample	2,833	7,365	3,088
	Barnes scattering components (odd, dbl, vol)	Training Sample	5,672	14,825	6,278
		Testing Sample	2,833	7,365	3,088
	Cloude scattering components (odd, dbl, vol)	Training Sample	5,672	14,825	6,278
		Testing Sample	2,833	7,365	3,088
6	**Sensor/Satellite- RISAT 1, 08-09-2016**				
	Parameter	Class	Vegetation	Urban	Water
	Raney Scattering Components (odd, dbl, vol)	Training Sample	9,408	24,508	10,376
		Testing Sample	4,683	12,175	5,104

the individual classes. The size of the training sample for each class was different. The multifrequency and multi-temporal SAR datasets were used; the land cover may change from 2008 to 2017. Therefore, training pixel was collected carefully for each class for each sensor's datasets; the spatial resolution of each dataset was different, which caused variation in the training sample size collected for each dataset. The details of the training pixels used for the classification of Pauli, Barnes, Cloude, and Raney scattering components are given in **Table 2**.

Confusion Matrix and Accuracy Assessments

The accuracy of the LULC classification images was evaluated based on the error matrix approach (Lillesand and Kiefer, 1979;

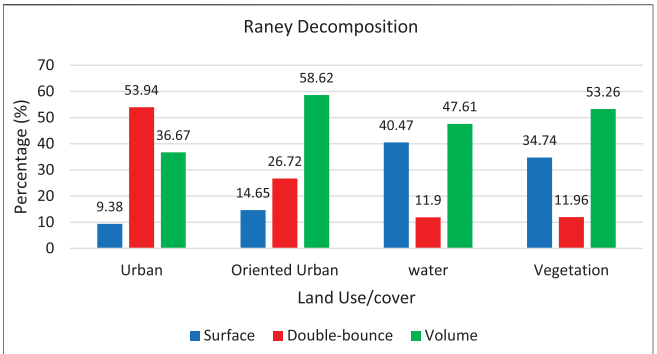

FIGURE 5 | Scattering response for urban, oriented urban, and water (smooth) scatterer obtained from Raney decomposition.

Congalton, 1991). It is the most effective method for analyzing classification accuracy. The error matrix, also referred to as the confusion matrix, compares the data (pixels) of each category/class of the classification result image with the ground reference data (pixels) to evaluate the accuracy. The error matrix provides descriptive measures such as overall accuracy (OA), user's accuracy (U.A), producer's accuracy (P.A), commission error, omission error, and kappa coefficient (k_c) to characterize the misclassification of the data (pixels). The overall accuracy (O.A) is the ratio of the total number of correctly classified pixels and the total number of referenced pixels (**Eq. 25**). The producer's accuracy (P.A) shows the accuracy of an individual class; it is the ratio of correctly classified pixels of a class (say A) to the total number of ground reference pixels of that class (**Eq. 26**); the user accuracy (U.A) shows the reliability of a map; it is the ratio of the correct pixel of a class (say "A") to the total number of pixels of that class (**Eq. 27**). The commission error (**Eq. 28**) describes the pixels that originally belong to the other classes ("B or C") and are wrongly included or categorized into a particular class ("A"). It is used to measure the error in "producer accuracy." The omission error describes the pixels that originally belong to a particular class ("A") but are omitted or excluded from that original class (**Eq. 29**). It describes the error in the "user's accuracy."

$$O.A\ (\%) = \frac{total\ number\ of\ correctly\ classified\ pixels}{total\ number\ of\ reference\ pixels} \times 100 \tag{25}$$

$$P.A = \frac{total\ number\ of\ correctly\ classified\ pixels\ of\ class\ "A"}{total\ number\ of\ reference\ pixels\ of\ class\ "A"} \times 100 \tag{26}$$

$$U.A = \frac{total\ number\ of\ correctly\ classified\ pixels\ of\ class\ "A"}{total\ number\ of\ classified\ pixels\ of\ class\ "A"} \times 100 \tag{27}$$

$$Commission\ error\ (\%) = 100 - P.A \tag{28}$$

$$Omission\ error\ (\%) = 100 - U.A \tag{29}$$

The KAPPA is a multivariate approach for the accuracy assessment, and its results are based on the KHAT statistics (k_c) (Congalton, 1991). The KHAT statistics (**Eq. 30**) measures

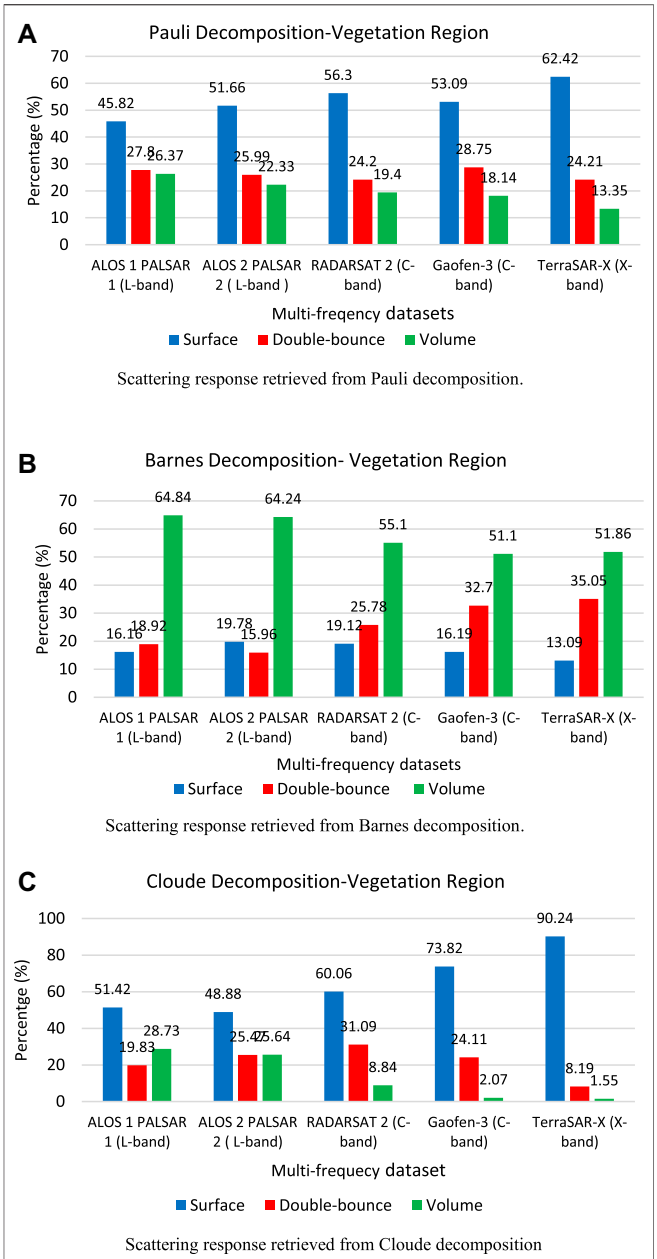

FIGURE 6 | Scattering response for vegetation structure obtained from Pauli, Barnes, and Cloude decomposition models. **(A)** Scattering response retrieved from Pauli decomposition. **(B)** Scattering response retrieved from Barnes decomposition. **(C)** Scattering response retrieved from Cloude decomposition.

the difference between "true agreement" (observed accuracy) and the "chance agreement." The "true agreement" refers to the precision between reference data and the classifier, whereas "chance agreement" shows precision between reference data and random classifier. The value of k_c ranges from "0" to "1"; $k_c \rightarrow 0$ shows no agreement; $k_c \rightarrow 1$, shows strong agreement. The value of k_c corresponds to the percentage of correct values due to "true agreement" *versus* "chance agreement" of the error matrix (Lillesand and Kiefer, 1979). Hence, the KAPPA

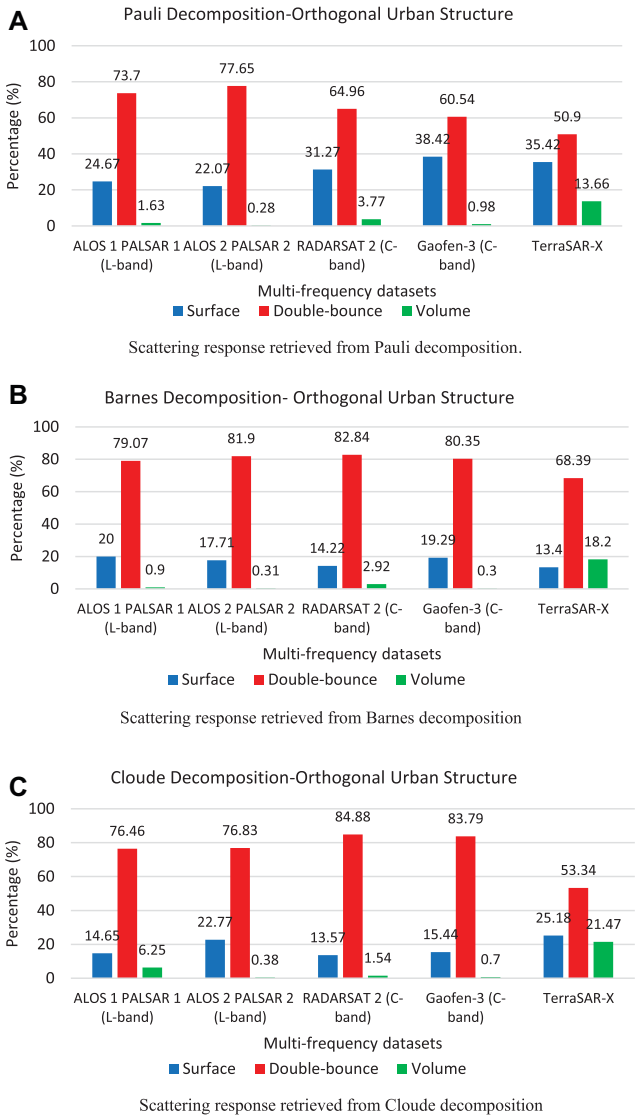

FIGURE 7 | Backscattering response for orthogonal urban structure obtained from Pauli, Barnes, and Cloude decomposition models. **(A)** Scattering response retrieved from Pauli decomposition. **(B)** Scattering response retrieved from Barnes decomposition. **(C)** Scattering response retrieved from Cloude decomposition.

coefficient indicates the extent to which the classification results are expressed by the error matrix better than the random results.

$$k_c = \frac{observed\ accuracy - chance\ agreement}{1 - chance\ agreement} \tag{30}$$

The ground reference data or testing sample for each class, *i.e.*, vegetation, urban, and waterbody, was collected from the Google Earth platform. The historical optical images of Google Earth were coordinated to the date of acquisition of SAR datasets to collect the ground reference data. The sampling technique and size are important considerations for collecting the testing sample (Lillesand and Kiefer, 1979). The stratified random sampling technique was used to collect the testing samples, representing each land cover as strata. The study area consists of a variety of features. The testing samples were collected for all the features representing each class. The sample size of the testing pixels was half of the training pixels for each class. The description of the testing sample used for the accuracy assessment of each LULC image is shown in **Table 2**. The confusion matrix was produced to derive overall accuracy (O.A.) and kappa coefficient (k_c) commission error (C.E.), omission error (O.E.) for each LULC classified image; the O.A., k_c, was used to determine the accuracy of LULC images, and C. E and O. E were used to determine the error of individual LULC classification.

The presence of heterogeneous features in the study area and disproportionate LULC caused an imbalanced number of training pixels for individual classes. This study utilized multifrequency and multi-temporal SAR data of different

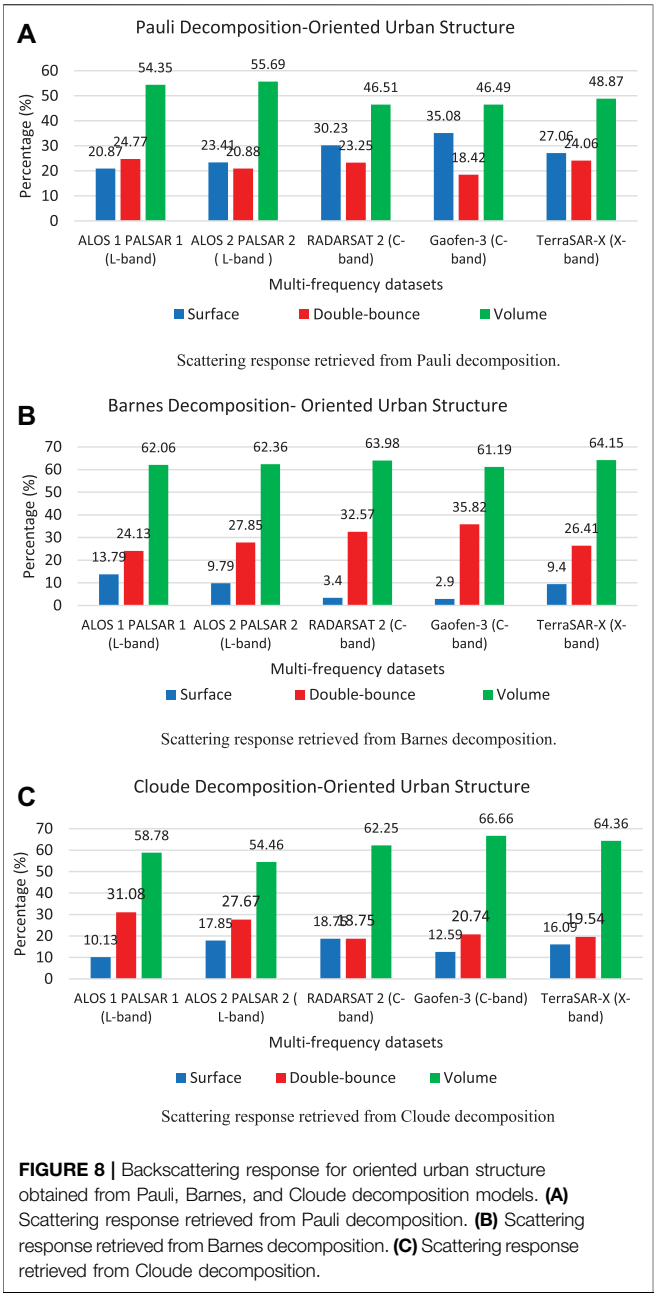

FIGURE 8 | Backscattering response for oriented urban structure obtained from Pauli, Barnes, and Cloude decomposition models. **(A)** Scattering response retrieved from Pauli decomposition. **(B)** Scattering response retrieved from Barnes decomposition. **(C)** Scattering response retrieved from Cloude decomposition.

sensors that caused imbalanced training sample sizes for each sensor's dataset (**Table 2**). The training sample size (the number of pixels) was significantly reduced for the low spatial resolution PolSAR datasets (*i.e.*, ALOS-1 PALSAR-1) than for high spatial resolution datasets (*i.e.*, TerraSAR-X, RISAT-1). The overall accuracy of the classification is influenced by the training sample size used by the classifier. However, several studies showed (Foody et al., 2006; Qian et al., 2015; Heydari and Mountrakis, 2018; Thanh Noi and Kappas, 2018) that the classification accuracy produced by the SVM classifier is least sensitive to the training sample size. The SVM creates the hyperplane or decision boundary based on support vectors instead of using all the training sample data. Therefore, the training sample size does not affect the SVM classification accuracy. A study by Qian et al. (2015) illustrated that the classification accuracy of the SVM classifier was significantly higher than the decision tree and k-nearest neighbor classifier, even for the small training sample data. Similarly, Thanh Noi and Kappas (2018) compared the effect of different training sample sizes for imbalanced and balanced training sample data using SVM, random forest, and k-nearest neighbor classifiers. They demonstrated that the imbalanced training sample data had the least impact on the SVM classifier's classification accuracy.

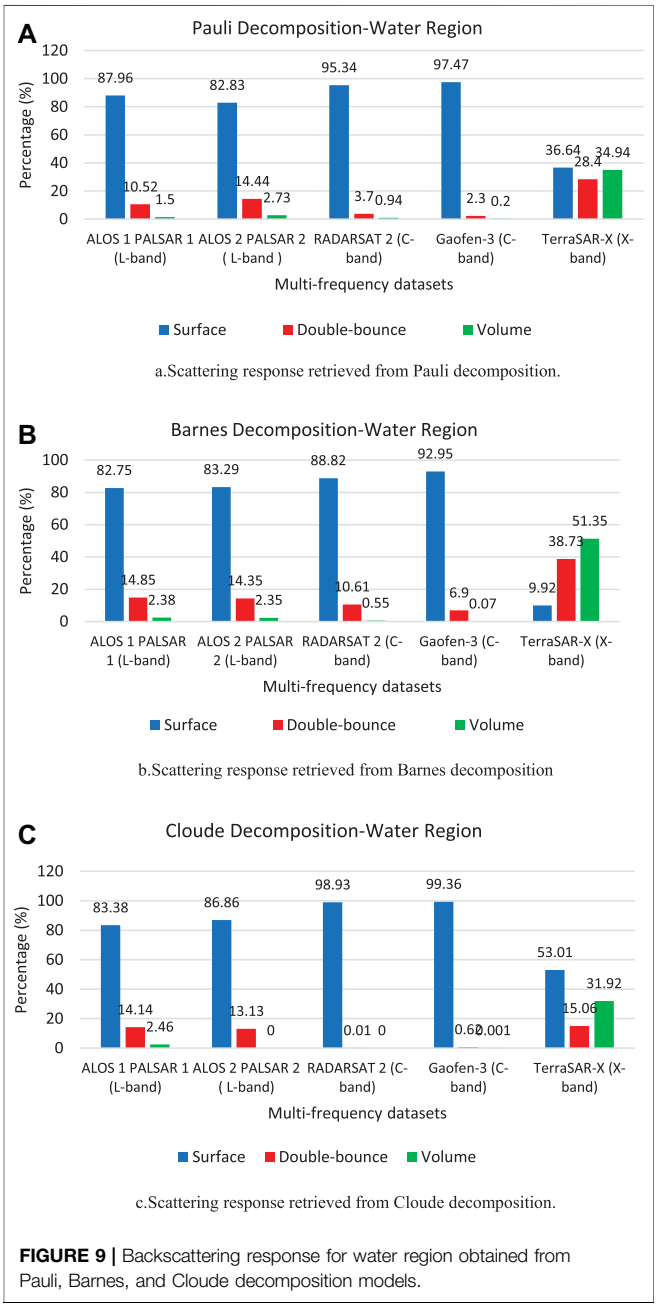

FIGURE 9 | Backscattering response for water region obtained from Pauli, Barnes, and Cloude decomposition models.

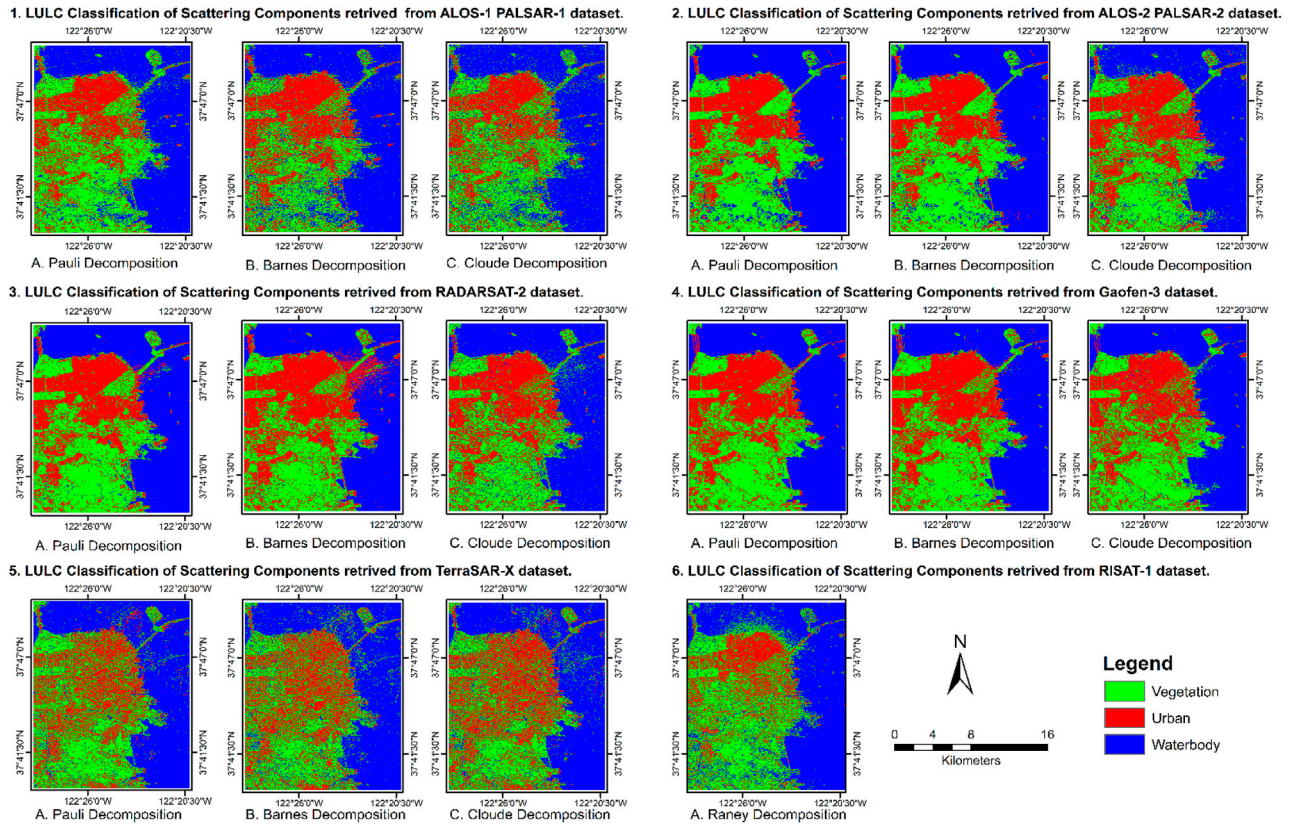

FIGURE 10 | LULC images obtained from classification of Pauli, Barnes, Cloude scattering components extracted from multi-temporal and multifrequency datasets; *Green*—vegetation, *Red*—urban, and *Blue*—waterbody.

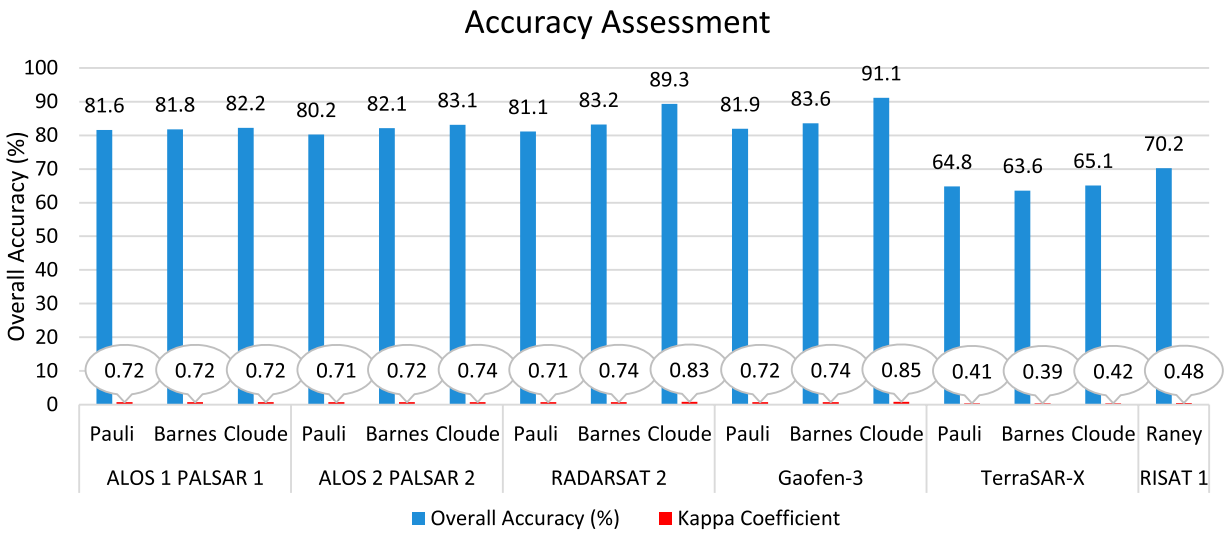

FIGURE 11 | Overall accuracy, kappa coefficient (k_c), of LULC images obtained from Pauli, Barnes, Cloude, and Raney decomposition models using multifrequency and multi-temporal datasets.

TABLE 3 | Overall Accuracy (O.A), kappa coefficient (k_c), commission (C.E.), and omission error (O.E.) of LULC images displayed in **Figure 10**.

1			**ALOS-1 PALSAR-1**			
		Class	C.E. (%)	O.E. (%)	O.A. (%)	k_c
	Pauli	Vegetation	49.25	28.11	81.6	0.72
		Urban	2.46	37.49		
		Water	12.63	4.64		
	Barnes	Vegetation	47.95	7.61	81.8	0.72
		Urban	7.02	35.50		
		Water	6.40	4.52		
	Cloude	Vegetation	46.06	13.61	82.2	0.72
		Urban	7.23	20.34		
		Water	6.84	1.06		
2			**ALOS-2 PALSAR-2**			
		Class	C.E. (%)	O.E. (%)	O.A. (%)	k_c
	Pauli	Vegetation	54.74	34.76	80.2	0.71
		Urban	2.46	37.90		
		Water	11.10	0.00		
	Barnes	Vegetation	53.70	6.42	82.1	0.72
		Urban	3.17	35.65		
		Water	0.00	0.00		
	Cloude	Vegetation	50.53	13.46	83.1	0.74
		Urban	5.32	29.37		
		Water	10.17	0.00		
3			**RADARSAT-2**			
		Class	C.E. (%)	O.E. (%)	O.A. (%)	k_c
	Pauli	Vegetation	54.64	40.00	81.1	0.71
		Urban	0.17	32.39		
		Water	20.30	0.00		
	Barnes	Vegetation	47.97	10.14	83.2	0.74
		Urban	5.48	26.69		
		Water	0.00	7.44		
	Cloude	Vegetation	36.58	19.71	89.3	0.83
		Urban	1.06	17.29		
		Water	4.81	0.00		
4			**Gaofen-3**			
		Class	C.E (%)	O.E. (%)	O.A (%)	k_c
	Pauli	Vegetation	52.66	35.37	81.9	0.72
		Urban	6.73	31.22		
		Water	17.20	0.00		
	Barnes	Vegetation	49.29	7.05	83.6	0.74
		Urban	10.24	23.74		
		Water	0.53	0.00		
	Cloude	Vegetation	23.56	24.34	91.1	0.85
		Urban	7.79	9.35		
		Water	3.33	0.00		
5			**TerraSAR-X**			
		Class	C.E. (%)	O.E. (%)	O.A. (%)	k_c
	Pauli	Vegetation	54.31	8.23	64.8	0.41
		Urban	3.71	48.09		
		Water	43.62	11.37		
	Barnes	Vegetation	55.15	13.41	63.6	0.39
		Urban	4.64	47.54		
		Water	53.37	13.95		
	Cloude	Vegetation	3.68	45.84	65.1	0.42
		Urban	51.19	12.43		
		Water	63.51	11.43		
6			**RISAT-1**			
		Class	C.E. (%)	O.E. (%)	O.A. (%)	k_c
	Raney	Vegetation	49.70	9.95	70.2	0.48
		Urban	2.43	35.21		
		Water	59.46	11.14		

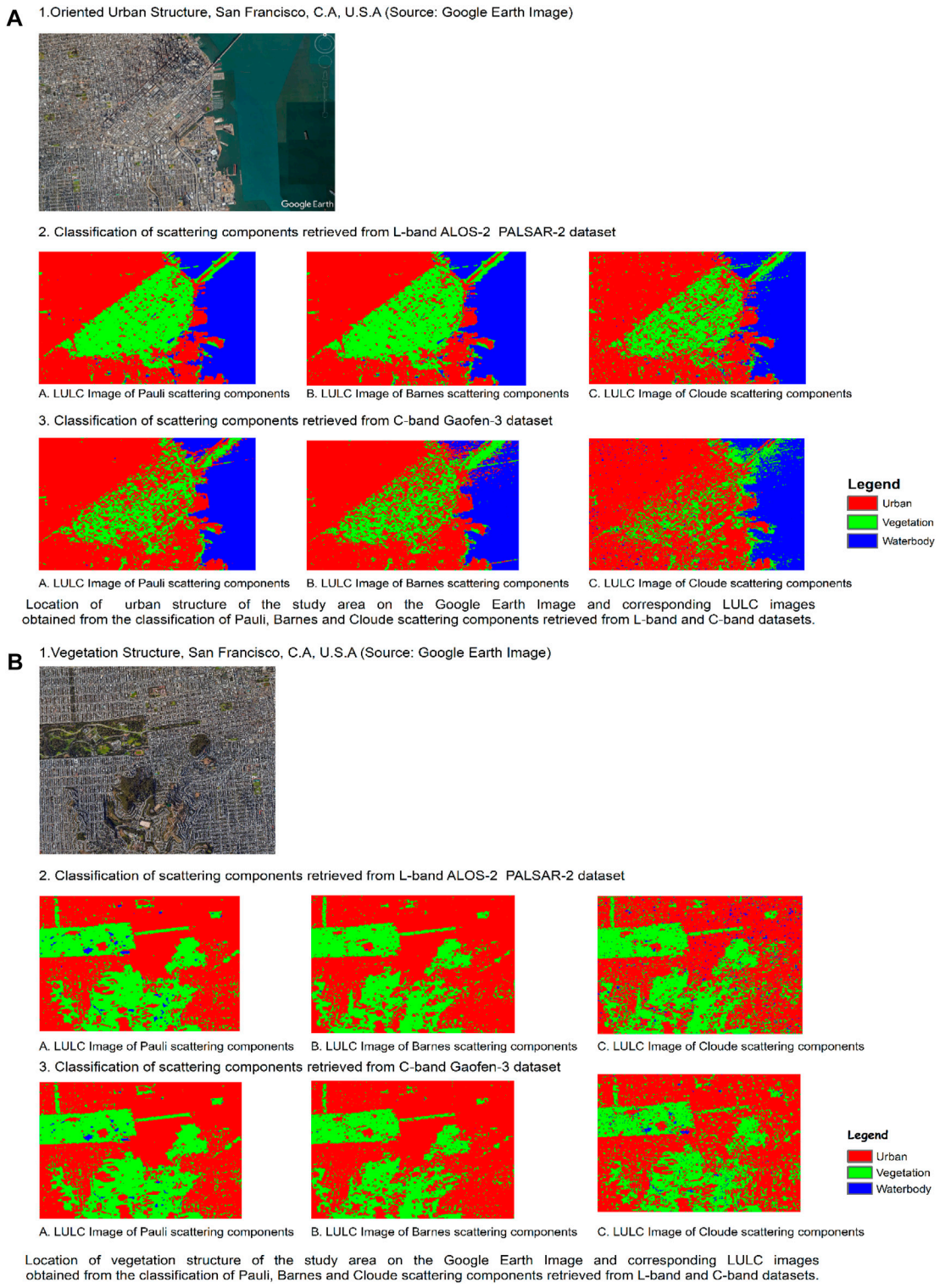

FIGURE 12 | Location of vegetation structure and urban structure of study area on Google Earth Image and corresponding LULC images obtained from classification of Pauli, Barnes, and Cloude scattering components retrieved from L-band and C-band datasets.

RESULT AND DISCUSSION

Comparison of Scattering Response for Vegetation, Urban, and Waterbody

The volume, double-bounce, and surface scattering responses retrieved from decomposition models were measured for the water, urban, and vegetation regions. The selected test area for the analysis is shown in **Figures 1** and **3**.

Vegetation

Figure 6 shows the scattering response for vegetation structure of decomposition models using multi-temporal and multifrequency datasets. The vegetation or forest canopy structure exhibited the volume scattering response due to multiple interactions with the branches, leaves, and tree trunks for the transmitted EM signals. The Pauli decomposition displayed the highest contribution to surface scattering response. The scattering components were coherent; therefore, it was suitable for the characterization of the homogeneous target within a single SAR resolution cell, hence failing to provide suitable scattering information. The Barnes decomposition displayed favorable results for the vegetation structure. The best volume scattering response was observed for L-band datasets due to its ability to penetrate the vegetation structure. However, the Cloude scattering components based on the eigenvalue–eigenvector approach failed to describe the appropriate scattering mechanism. It displayed a surface scattering response. The Raney decomposition model showed reliable information for vegetation structure. It displayed the highest contribution to volume scattering for CP datasets (**Figure 5**).

The roll-invariant decomposition model was suitable for the study of vegetation structure (**Figure 6B**). The small contribution to surface scattering response in the vegetation region showed the interaction of emitted radar signal with the ground/smooth surface. Similarly, even-bounce scattering contribution illustrated the interaction between ground and tree trunks. From **Figure 6**, the volume scattering response associated with the vegetation cover was more intense for the longer wavelength (L-band). The intensity of volume scattering decreased for the shorter wavelength (X-band) because the penetration capacity of EM wave decreases with an increase in frequency. It shows that a low-frequency or longer wavelength dataset is more suitable for the study of vegetation or forest structures.

Urban Region

The urban structure is described as a dihedral structure that produces a double-bounce (even) scattering response for the incoming SAR sensor's EM radiations. In this study, the chosen test area for urban region consists of orthogonal urban structure and oriented urban structure; the scattering response was measured for both types of structures and shown in **Figures 7** and **8**.

All the decomposition models provided reliable information for the orthogonal urban structure and illustrated the dominance of the double-bounce scattering response. The best double-bounce scattering response was obtained from Cloude and Barnes decomposition models using C-band datasets (RADARSAT-2, Gaofen-3). The Cloude and Barnes scattering components were roll-invariant, useful for characterizing the urban structure using C-band datasets. The Pauli scattering components were coherent, which was favorable for studying homogeneous structures. The Raney decomposition models showed a double-bounce scattering response for the CP RISAT-1 dataset.

For oriented urban structures, all the decomposition models overestimated volume scattering response and displayed the least contribution to double-bounce scattering response. From **Figure 8**, the Pauli decomposition displayed minimum contribution to the double-bounce scattering power. The Barnes decomposition improved the double-bounce scattering response to some extent, whereas Cloude decomposition reduced the volume scattering contribution. Similarly, the Raney decomposition model displayed volume scattering response for oriented urban structures (**Figure 5**). All the decomposition models failed to describe the appropriate scattering mechanism for oriented urban structure.

Water Region

The result of the scattering response retrieved from decomposition modeling approaches for water region is displayed in **Figure 9**. The water surface illustrates smooth or Bragg's scatterer type, producing odd-bounce or surface scattering response for the transmitted EM wave. All the decomposition models described surface scattering response for water region using L-band and C-band datasets. The Raney decomposition displayed a higher contribution to volume scattering response than surface scattering response for waterbody (smooth surface) using CP datasets (**Figure 5**). The Cloude and Barnes displayed enhanced surface scattering response for ALOS-2 PALSAR-2 and Gaofen-3 due to an increase in spatial resolution of the datasets (**Figure 9**).

All the decomposition models displayed the lowest surface scattering contribution for the waterbody using TerraSAR-X datasets. The Pauli and Barnes decomposition underestimated surface scattering mechanism and overestimated volume scattering response, whereas Cloude decomposition displayed surface scattering contribution. The low-frequency dataset provided very less scattering information for the characterization of smooth structures.

Comparison Land Use/Land Cover Classification of Scattering Components

Figure 10 represents the LULC images obtained from the classification of Pauli, Barnes, Cloude, and Raney scattering components (**Figure 3**), which were retrieved from the multifrequency PolSAR datasets, and **Table 3** shows their accuracy assessment.

Classification of Scattering Components Retrieved From L-Band ALOS-1 PALSAR-1 and ALOS-2 PALSAR-2 Datasets

The classification of the Pauli scattering component displayed O.A. values of 81.6% ($k_c = 0.72$) and 80.2% ($k_c = 0.71$) for ALOS-1 PALSAR-1 and ALOS-2 PALSAR-2, respectively. The Pauli decomposition described the highest surface scattering

contribution than volume scattering for vegetation structure (**Figure 6A**), which led to misclassification of vegetation pixels into water class. The Barnes decomposition model appropriately defined the volume scattering mechanism for vegetation structure and the double-bounce scattering response for urban structure than the Pauli decomposition model. The Barnes scattering components showed better O.A. in the classification: 81.8% (k_c = 0.72) and 82.1% (k_c = 0.72) for ALOS-1 PALSAR-1 and ALOS-2 PALSAR-2 datasets, respectively, than Pauli scattering components. The Cloude decomposition model demonstrated a remarkable scattering mechanism for the smooth surface (waterbody) and dihedral (orthogonal urban) structures. This approach minimized the volume scattering response for oriented urban buildings. Therefore, the classification of Cloude scattering components improved the O.A. to 82.2% (k_c = 0.72) and 83.1% (k_c = 0.74) for ALOS-1 PALSAR-1 and ALOS-2 PALSAR-2 datasets, respectively. However, vegetation pixels were misclassified into the water class because this model had displayed a dominant surface scattering response for vegetation.

Classification of Scattering Components Retrieved From C-Band RADARSAT-2 and Gaofen-3 Datasets

The targets had demonstrated favorable scattering responses for C-band datasets. The Barnes and Cloude decomposition models displayed relatively good scattering responses to characterize dihedral (orthogonal) structures and smooth surfaces (waterbody) for C-band than the L-band datasets, which eventually increases the O.A. of the LULC classification. The Pauli decomposition displayed a relatively lower double-bounce scattering response for oriented urban structure for the C-band than the L-band datasets; therefore, it presented low accuracy in the classification. The classification of coherent scattering component of Pauli decomposition displayed O.A. values of 81.1% (k_c = 0.71) and 81.9% (k_c = 0.72) for RADARSAT-1 and Gaofen-3 dataset, respectively. The roll-invariant scattering component of Barnes decomposition showed better O.A. than Pauli decomposition in the classification, *i.e.*, 83.2% (k_c = 0.74) and 83.6% (k_c = 0.74) for RADARSAT-2 and Gaofen-3 datasets, respectively. The highest O.A. values were achieved from the classification of Cloude scattering components—89.3% (k_c = 0.83) and 91.1% (k_c = 0.85) for RADARSAT-2 and Gaofen-3 datasets, respectively (**Table 3**).

Classification of Scattering Components Retrieved From TerraSAR-X Dataset

As shown in **Table 3**, the classification of Pauli scattering components presented an O.A. of 64.8% (k_c = 0.41), the roll-invariant scattering components of Barnes decomposition displayed an O.A. of63.6% (k_c = 0.39), and the Cloude scattering components presented an O.A. of 65.1% (k_c = 0.42).

The Pauli,Barnes, and Cloude decomposition models demonstrated the least reliable scattering information to identify the target for TerraSAR-X datasets. Eventually, the classification of scattering components presented the least overall accuracy in the classification. The Pauli decomposition displayed an underestimation of the volume scattering mechanism for vegetation structure. The Barnes decomposition underestimated surface scattering response for the water region. The Cloude decomposition misinterpreted the vegetation structure as a smooth scatterer. Therefore, the error was highest for each class (**Table 3**) due to the misinterpretation of the targets.

Classification of Scattering Components Retrieved From Compact-Pol RISAT-1 Dataset

The Raney decomposition model showed suitable scattering information about the orthogonal urban structure and vegetation region. However, it underestimated the surface scattering mechanism for the smooth scatterer (waterbody) and double-bounce scattering response for oriented urban structures. Hence, the accuracy of water and the urban class was low due to misinterpretation of the target. The Raney scattering components presented an O.A. of 70.2% (k_c = 0.48) in the classification.

The coherent decomposition models are suitable for the study of "pure targets" or homogeneous targets within a single resolution cell, and incoherent decomposition models are favorable for the study of "distributed targets" or heterogeneous targets. The classification of Cloude and Barnes scattering components showed higher O.A. than Pauli scattering components (**Figure 11**). All the decomposition models overestimated the volume scattering mechanism for oriented urban structure, which led to the misclassification of the urban pixels into vegetation class. Therefore, the omission error was highest for the urban class, and the commission error was highest for the vegetation class in the output LULC images. The water class presented the lowest error in the classification because all the decomposition models appropriately described the surface scattering mechanism for the waterbody (**Table 3**).

The roll-invariant Barnes and Cloude decomposition models demonstrated a relatively better double-bounce scattering mechanism for orthogonal structure using C-band datasets than L-band (**Figures 7B,C**). Therefore, the C-band dataset displayed higher accuracy for the urban class than the L-band datasets (**Figure 12A**) in the classification. The roll-invariant Barnes decomposition provided desirable scattering information for the characterization of vegetation structure using C-band datasets (**Figure 6B**), presenting good accuracy for the classification of the vegetation class (**Figure 12B**).

CONCLUSION

The main objective of this study was to use multifrequency spaceborne SAR data that were acquired over San Francisco City from the years 2008–2017. This study explored and compared the classification outputs of multifrequency spaceborne PolSAR data. The classification schemes were performed for scattering-based characterization of LULC using multifrequency SAR sensor's ALOS-1 PALSAR-1, ALOS-2 PALSAR-2, RADARSAT-2, Gaofen-3, TerraSAR-X, and RISAT-1 dataset. The coherent-based Pauli

decomposition model demonstrated reliable scattering information for "pure target" within a single cell such as a homogeneous waterbody and orthogonal urban structures. The roll-invariant Barnes decomposition provided fruitful scattering information for vegetation and urban structure. The eigenvalue–eigenvector-based Cloude decomposition model described a favorable scattering mechanism for the characterization of urban and waterbody. These decomposition modeling approaches failed to provide reliable scattering information to characterize oriented urban structures. The CP Raney decomposition provided desirable scattering information for vegetation and orthogonal urban structure. The classification of Raney scattering components presented 70.2% (k_c = 0.48) O.A. The Pauli, Barnes, and Cloude decomposition models presented better scattering information for C-band datasets than L-band datasets. Therefore, the O.A. for the classification was higher for C-band than the L-band datasets. The highest O.A. was achieved from the classification of Cloude scattering components, *i.e.*, 89.3% (k_c = 0.83) and 91.1% (k_c = 0.85) for the RADARSAT-2 and Gaofen-3 datasets, respectively. The decomposition models showed the least reliable scattering information for the TerraSAR-X dataset. Therefore, the classification of scattering components presented the least O.A. The Barnes scattering components had shown the least O.A., *i.e.*, 63.6% (k_c = 0.39) for the TerraSAR-X dataset. The decomposition models misinterpreted the oriented urban structure as vegetation that caused misclassification. This work aimed to implement a machine learning algorithm for LULC classification from polarimetric parameters of PolSAR multisensor data. The findings of this work show the significance of machine learning algorithms on multisensor, multifrequency, and multi-polarization data as compared with the classification work done in the previous study. By analyzing the results of polarimetric decompositions, it is also observed that there is a requirement of rotationally invariant scattering elements based on a higher-order decomposition model to achieve higher accuracy with classification results.

DATA AVAILABILITY STATEMENT

The original contributions presented in the study are included in the article/Supplementary Material, further inquiries can be directed to the corresponding author.

AUTHOR CONTRIBUTIONS

Writing—original draft preparation, SV; conceptualization, SK and SV; satellite data acquisition, SK; software, SK; methodology, SK; writing—review and editing, SV, SK, VM, and RR; supervision of the project, SK and VM; visualization SV, SK, VM, and RR.

ACKNOWLEDGMENTS

The authors are thankful to the German Aerospace Center (DLR) Oberpfaffenhofen for providing TerraSAR-X data to SK under the Project Id -NTI_POLI6635 on PolInSAR Tomography for above ground biomass estimation. The authors would like to express their sincere gratitude to the whole research team of ESA for providing SNAP 8.0 and the Polarimetric SAR data Processing and Educational Toolbox PolSARPro 6.0.3 (Biomass Edition) tools for polarimetric processing of the SAR data. The authors are grateful to the Institute of Electronics and Telecommunications of Rennes (IETR), Rennes, France, for maintaining the portal to download the PolSAR data (RISAT-1, ALOS-1 PALSAR-1, ALOS-2 PALSAR-2, GAOFEN-3, and RADARSAT-2) for San Francisco City and the software/tool PolSARPro 6.0.3.

REFERENCES

Agrawal, N., Kumar, S., and Tolpekin, V. (2016). Polarimetric SAR Interferometry-Based Decomposition Modelling for Reliable Scattering Retrieval. *SPIE Proceedings,Land Surf. Cryosphere Remote Sensing.* 9877, 31–40. doi:10.1117/12.2223977

Alberga, V. (2007). A Study of Land Cover Classification Using Polarimetric SAR Parameters. *Int. J. Remote Sensing.* 28, 3851–3870. doi:10.1080/01431160601075541

Ali, Z., Kroupnik, G., Matharu, G., Graham, J., Barnard, I., Fox, P., et al. (2014). RADARSAT-2 Space Segment Design and its Enhanced Capabilities with Respect to RADARSAT-1. *Can. J. Remote Sensing.* 30, 235–245. doi:10.5589/M03-077

ArcGIS Desktop | Download and Documentation (2022). Available at: https://www.esri.com/en-us/arcgis/products/arcgis-desktop/resources (Accessed January 3, 2022).

Awasthi, S., Thakur, P. K., Kumar, S., Kumar, A., Jain, K., and Mani, S. (2020). Snow Density Retrieval Using Hybrid Polarimetric RISAT-1 Datasets. IEEE J. Sel. Top. Appl. Earth Obs. *Remote Sens.* 13, 3058–3065. doi:10.1109/JSTARS.2020.2991156

Babu, A., Kumar, S., and Agrawal, S. (2021a). Polarimetric Calibration and Spatio-temporal Polarimetric Distortion Analysis of UAVSAR PolSAR Data. *Earth Space Sci.* 8, e2020EA001629. doi:10.1029/2020EA001629

Babu, A., Kumar, S., and Agrawal, S. (2021b). Polarimetric Calibration of L-Band UAVSAR Data. *J. Indian Soc. Remote Sens.* 49, 541–549. doi:10.1007/s12524-020-01241-1

Babu, A., Kumar, S., and Agrawal, S. (2019a). Polarimetric Calibration of RISAT-1 Compact-Pol Data. *IEEE J. Sel. Top. Appl. Earth Observations Remote Sensing.* 12, 3731–3736. doi:10.1109/jstars.2019.2932019

Babu, A., Kumar, S., and Agrawal, S. (2019b). RISAT-1 Compact Polarimetric Calibration and Decomposition. *Proceedings.* 18, 3. doi:10.3390/ECRS-3-06189

Bai, Y., Sun, G., Li, Y., Ma, P., Li, G., and Zhang, Y. (2021). Comprehensively Analyzing Optical and Polarimetric SAR Features for Land-Use/land-Cover Classification and Urban Vegetation Extraction in Highly-Dense Urban Area. *Int. J. Appl. Earth Observation Geoinformation.* 103, 102496. doi:10.1016/j.jag.2021.102496

Bhanu Prakash, M., and Kumar, S. (2021a). Multifrequency Analysis of PolInSAR-Based Decomposition Using Cosine-Squared Distribution. *IETE Tech. Rev.* 0, 1–8. doi:10.1080/02564602.2021.1892542

Bhanu Prakash, M., and Kumar, S. (2021b). PolInSAR Decorrelation-Based Decomposition Modelling of Spaceborne Multifrequency SAR Data. *Int. J. Remote Sensing.* 42, 1398–1419. doi:10.1080/01431161.2020.1829155

Bhattacharya, A., Muhuri, A., De, S., Manickam, S., and Frery, A. C. (2015). Modifying the Yamaguchi Four-Component Decomposition Scattering Powers Using a Stochastic Distance. *IEEE J. Sel. Top. Appl. Earth*

Observations Remote Sensing. 8, 3497–3506. doi:10.1109/jstars.2015.2420683

Bole, A., Wall, A., and Norris, A. (2014). *"Chapter 3-Target Detection," in Radar and ARPA Manual*. Editors A. Bole, A. Wall, and A. Norris. Third Edition (Oxford: Butterworth-Heinemann), 139–213. doi:10.1016/B978-0-08-097752-2.00003-9

Boser, B. E., Guyon, I. M., and Vapnik, V. N. (1992). "Training Algorithm for Optimal Margin Classifiers," in Proceedings of the Fifth Annual ACM Workshop on Computational Learning Theory COLT '92 (New York, NY: Association for Computing Machinery), 144–152. doi:10.1145/130385.130401

Brusch, S., Lehner, S., Fritz, T., Soccorsi, M., Soloviev, A., and van Schie, B. (2011). Ship Surveillance with TerraSAR-X. *IEEE Trans. Geosci. Remote Sensing.* 49, 1092–1103. doi:10.1109/tgrs.2010.2071879

Buono, A., Nunziata, F., Migliaccio, M., Yang, X., and Li, X. (2017). Classification of the Yellow River delta Area Using Fully Polarimetric SAR Measurements. *Int. J. Remote Sensing.* 38, 6714–6734. doi:10.1080/01431161.2017.1363437

Chaudhary, V., and Kumar, S. (2021). Dark Spot Detection for Characterization of marine Surface Slicks Using UAVSAR Quad-Pol Data. *Sci. Rep.* 11, 8975. doi:10.1038/s41598-021-88301-9

Chaudhary, V., and Kumar, S. (2020). Marine Oil Slicks Detection Using Spaceborne and Airborne SAR Data. *Adv. Space Res.* 66, 854–872. doi:10.1016/j.asr.2020.05.003

Chaussard, E., Amelung, F., Abidin, H., and Hong, S.-H. (2013). Sinking Cities in Indonesia: ALOS PALSAR Detects Rapid Subsidence Due to Groundwater and Gas Extraction. *Remote Sensing Environ.* 128, 150–161. doi:10.1016/j.rse.2012.10.015

Chen, S.-W., Li, Y.-Z., Wang, X.-S., Xiao, S.-P., and Sato, M. (2014a). Modeling and Interpretation of Scattering Mechanisms in Polarimetric Synthetic Aperture Radar: Advances and Perspectives. *IEEE Signal. Process. Mag.* 31, 79–89. doi:10.1109/msp.2014.2312099

Chen, S. W., Xue-Song Wang, X. S., Yong-Zhen Li, Y. Z., and Sato, M. (2014b). Adaptive Model-Based Polarimetric Decomposition Using Polinsar Coherence. *IEEE Trans. Geosci. Remote Sensing.* 52, 1705–1718. doi:10.1109/tgrs.2013.2253780

Chen, S.-W., and Sato, M. (2013). Tsunami Damage Investigation of Built-Up Areas Using Multitemporal Spaceborne Full Polarimetric SAR Images. *IEEE Trans. Geosci. Remote Sensing.* 51, 1985–1997. doi:10.1109/tgrs.2012.2210050

Chen, S.-W., Wang, X.-S., Xiao, S.-P., and Sato, M. (2018). "Fundamentals of Polarimetric Radar Imaging and Interpretation," in *Target Scattering Mechanism in Polarimetric Synthetic Aperture Radar: Interpretation and Application* (Singapore: Springer Singapore), 1–42. doi:10.1007/978-981-10-7269-7_1

Cloude, S. R., Goodenough, D. G., and Chen, H. (2012). Compact Decomposition Theory. *IEEE Geosci. Remote Sensing Lett.* 9, 28–32. doi:10.1109/lgrs.2011.2158983

Cloude, S. R. (1985). Target Decomposition Theorems in Radar Scattering. *Electronics Lett.* 21, 22–24. doi:10.1049/el:19850018

Congalton, R. G. (1991). A Review of Assessing the Accuracy of Classifications of Remotely Sensed Data. *Remote Sensing Environ.* 37, 35–46. doi:10.1016/0034-4257(91)90048-B

ENVI® | Image Processing & Analysis Software (2022). Available at: https://www.l3harrisgeospatial.com/Software-Technology/ENVI (Accessed January 3, 2022).

Ferro-Famil, L., and Pottier, E. (2016). "1 - Synthetic Aperture Radar Imaging," in *Microwave Remote Sensing of Land Surface*. Editors N. Baghdadi and M. Zribi (Oxford: Elsevier), 1–65. doi:10.1016/B978-1-78548-159-8.50001-3

Foody, G. M., Mathur, A., Sanchez-Hernandez, C., and Boyd, D. S. (2006). Training Set Size Requirements for the Classification of a Specific Class. *Remote Sensing Environ.* 104, 1–14. doi:10.1016/j.rse.2006.03.004

Freeman, A., and Durden, S. L. (1998). A Three-Component Scattering Model for Polarimetric SAR Data. *IEEE Trans. Geosci. Remote Sensing* 36, 963–973. doi:10.1109/36.673687

Freeman, A. (2007). Fitting a Two-Component Scattering Model to Polarimetric SAR Data from Forests. *IEEE Trans. Geosci. Remote Sensing.* 45, 2583–2592. doi:10.1109/tgrs.2007.897929

Garg, R., Kumar, A., Prateek, M., Pandey, K., and Kumar, S. (2022). Land Cover Classification of Spaceborne Multifrequency SAR and Optical Multispectral Data using Machine Learning. *Adv. Space Res.* 69, 1726–1742. doi:10.1016/j.asr.2021.06.028

Heydari, S. S., and Mountrakis, G. (2018). Effect of Classifier Selection, Reference Sample Size, Reference Class Distribution and Scene Heterogeneity in Per-Pixel Classification Accuracy Using 26 Landsat Sites. *Remote Sensing Environ.* 204, 648–658. doi:10.1016/j.rse.2017.09.035

Holm, W. A., and Barnes, R. M. (1988). "On Radar Polarization Mixed Target State Decomposition Techniques," in *Decomposition Techniques* (IEEE), 249–254. doi:10.1109/nrc.1988.10967

Huynen, J. R. (1978). "Phenomenological Theory of Radar Targets," in *Electromagnetic Scattering*. Editor P. L. E. Uslenghi (New York: Academic Press), 653–712. doi:10.1016/B978-0-12-709650-6.50020-1

Jafari, M., Maghsoudi, Y., and Valadan Zoej, M. J. (2015). A New Method for Land Cover Characterization and Classification of Polarimetric SAR Data Using Polarimetric Signatures. *IEEE J. Sel. Top. Appl. Earth Observations Remote Sensing.* 8, 3595–3607. doi:10.1109/jstars.2014.2387374

Jordan, R. (1980). The Seasat-A Synthetic Aperture Radar System. *IEEE J. Oceanic Eng.* 5, 154–164. doi:10.1109/joe.1980.1145451

Kranjčić, N., Medak, D., Župan, R., and Rezo, M. (2019). Machine Learning Methods for Classification of the Green Infrastructure in City Areas. *Ijgi.* 8 (8), 463. doi:10.3390/IJGI8100463

Krogager, E. (1990). New Decomposition of the Radar Target Scattering Matrix. *Electron. Lett.* 26, 1525. doi:10.1049/el:19900979

Kumar, P., Gupta, D. K., Mishra, V. N., and Prasad, R. (2015). Comparison of Support Vector Machine, Artificial Neural Network, and Spectral Angle Mapper Algorithms for Crop Classification Using LISS IV Data. *Int. J. Remote Sensing* 36, 1604–1617. doi:10.1080/2150704X.2015.1019015

Kumar, S., Babu, A., Agrawal, S., Asopa, U., Shukla, S., and Maiti, A. (2022). Polarimetric Calibration of Spaceborne and Airborne Multifrequency SAR Data for Scattering-Based Characterization of Manmade and Natural Features. *Adv. Space Res.* 69, 1684–1714. doi:10.1016/j.asr.2021.02.023

Kumar, S., Garg, R. D., Govil, H., and Kushwaha, S. P. S. (2019). PolSAR-Decomposition-Based Extended Water Cloud Modeling for Forest Aboveground Biomass Estimation. *Remote Sensing* 11 (11), 2287. doi:10.3390/RS11192287

Kumar, S., Govil, H., Srivastava, P. K., Thakur, P. K., and Kushwaha, S. P. S. (2020). Spaceborne Multifrequency PolInSAR-Based Inversion Modelling for Forest Height Retrieval. *Remote Sensing* 12 (12), 4042. doi:10.3390/RS12244042

Lardeux, C., Frison, P.-L., Tison, C., Souyris, J.-C., Stoll, B., Fruneau, B., et al. (2009). Support Vector Machine for Multifrequency SAR Polarimetric Data Classification. *IEEE Trans. Geosci. Remote Sensing* 47, 4143–4152. doi:10.1109/tgrs.2009.2023908

Lee, J.-S., and Pottier, E. (2009). *Polarimetric Radar Imaging From Basics to Applications*. 1st Edn. Boca Raton: CRC Press, Taylor & Fancis Group. doi:10.1201/9781420054989

Lillesand, T. M., and Kiefer, R. W. (1979). *Remote Sensing and Image Interpretation*. 1st Edn. New York: John Wiley & Sons, Ltd.

Lu, D. (2007). A Survey of Image Classification Methods and Techniques for Improving Classification Performance. *Int. J. Remote Sensing* 28, 823–870. doi:10.1080/01431160600746456

Maghsoudi, Y. (2011). Analysis of Radarsat-2 Full Polarimetric Data for Forest Mapping. *Dep. Geomatics Eng. Univ. Calgary*. Degree PhD.

Mahmood, A. (1997). RADARSAT-1 Background Mission for a Global SAR Coverage. *Igarss'97. 1997 IEEE Int. Geosci. Remote Sensing Symp. Proc. Remote Sensing - A Scientific Vis. Sustainable Development* Vol. 3, 1217. doi:10.1109/IGARSS.1997.606402

Maiti, A., Kumar, S., Tolpekin, V., and Agarwal, S. (2021). A Computationally Efficient Hybrid Framework for Polarimetric Calibration of Quad-Pol SAR Data. *Earth Space Sci.* 8, e2020EA001447. doi:10.1029/2020EA001447

Mason, D. C., Speck, R., Devereux, B., Schumann, G. J.-P., Neal, J. C., and Bates, P. D. (2010). Flood Detection in Urban Areas Using TerraSAR-X. *IEEE Trans. Geosci. Remote Sensing* 48, 882–894. doi:10.1109/tgrs.2009.2029236

Mishra, V. N., Prasad, R., Kumar, P., Gupta, D. K., and Srivastava, P. K. (2017a). Dual-polarimetric C-Band SAR Data for Land Use/land Cover Classification by Incorporating Textural Information. *Environ. Earth Sci.* 76, 1. doi:10.1007/S12665-016-6341-7

Mishra, V. N., Prasad, R., Kumar, P., Srivastava, P. K., and Rai, P. K. (2017b). Knowledge-based Decision Tree Approach for Mapping Spatial Distribution of rice Crop Using C-Band Synthetic Aperture Radar-Derived Information. *J. Appl. Remote Sens.* 11, 1. doi:10.1117/1.JRS.11.046003

Mishra, V. N., Prasad, R., Rai, P. K., Vishwakarma, A. K., and Arora, A. (2019). Performance Evaluation of Textural Features in Improving Land Use/land Cover Classification Accuracy of Heterogeneous Landscape Using Multi-Sensor Remote Sensing Data. *Earth Sci. Inform.* 12, 71–86. doi:10.1007/S12145-018-0369-Z

Misra, T., and Kirankumar, A. S. (2014). "RISAT-1: Configuration and Performance Evaluation," in 2014 XXXIth URSI General Assembly and Scientific Symposium (URSI GASS) (Beijing: IEEE), 1–4. doi:10.1109/URSIGASS.2014.6929612

Misra, T., Rana, S. S., Desai, N. M., Dave, D. B., RajeevjyotiArora, R. K., et al. (2013). Synthetic Aperture Radar Payload On-Board RISAT-1: Configuration, Technology and Performance. *Curr. Sci.* 104, 446–461. Available at: https://www.currentscience.ac.in/Volumes/104/04/0446.pdf.

Morena, L. C., James, K. V., and Beck, J. (2004). V, and Beck, JAn Introduction to the RADARSAT-2 mission. *Can. J. Remote Sensing* 30, 221–234. doi:10.5589/m04-004

Ng, A. H.-M., Ge, L., Li, X., Abidin, H. Z., Andreas, H., and Zhang, K. (2012). Mapping Land Subsidence in Jakarta, Indonesia Using Persistent Scatterer Interferometry (PSI) Technique with ALOS PALSAR. *Int. J. Appl. Earth Observation Geoinformation* 18, 232–242. doi:10.1016/j.jag.2012.01.018

Niu, X., and Ban, Y. (2013). Multi-temporal RADARSAT-2 Polarimetric SAR Data for Urban Land-Cover Classification Using an Object-Based Support Vector Machine and a Rule-Based Approach. *Int. J. Remote Sensing* 34, 1–26. doi:10.1080/01431161.2012.700133

Orieschnig, C. A., Belaud, G., Venot, J.-P., Massuel, S., and Ogilvie, A. (2021). Input Imagery, Classifiers, and Cloud Computing: Insights from Multi-Temporal LULC Mapping in the Cambodian Mekong Delta. *Eur. J. Remote Sensing* 54, 398–416. doi:10.1080/22797254.2021.1948356

Pal, M., and Foody, G. M. (2010). Feature Selection for Classification of Hyperspectral Data by SVM. *IEEE Trans. Geosci. Remote Sensing* 48, 2297–2307. doi:10.1109/tgrs.2009.2039484

PolSARpro v6.0 (Biomass Edition) Toolbox Download – STEP (2022). Available at: https://step.esa.int/main/download/polsarpro-v6-0-biomass-edition-toolbox-download/(Accessed January 3, 2022).

Qi, Z., Yeh, A. G.-O., Li, X., and Lin, Z. (2012). A Novel Algorithm for Land Use and Land Cover Classification Using RADARSAT-2 Polarimetric SAR Data. *Remote Sensing Environ.* 118, 21–39. doi:10.1016/j.rse.2011.11.001

Qian, Y., Zhou, W., Yan, J., Li, W., and Han, L. (2015). Comparing Machine Learning Classifiers for Object-Based Land Cover Classification Using Very High Resolution Imagery. *Remote Sensing* 7, 153–168. doi:10.3390/rs70100153

Raney, R. K., Cahill, J. T. S., Patterson, G. W., and Bussey, D. B. J. (2012). Them-chidecomposition of Hybrid Dual-Polarimetric Radar Data with Application to Lunar Craters. *J. Geophys. Res.* 117, a–n. doi:10.1029/2011JE003986

Rawat, A., Kumar, A., Upadhyay, P., and Kumar, S. (2021). Deep Learning-Based Models for Temporal Satellite Data Processing: Classification of Paddy Transplanted fields. *Ecol. Inform.* 61, 101214. doi:10.1016/j.ecoinf.2021.101214

Rosen, P. A., Kim, Y., Kumar, R., Misra, T., Bhan, R., and Sagi, V. R. (2017). Global Persistent SAR Sampling with the NASA-ISRO SAR (NISAR) mission. *2017 IEEE Radar Conf. RadarConf* 2017, 0410–0414. doi:10.1109/radar.2017.7944237

Rosenqvist, A., Shimada, M., Ito, N., and Watanabe, M. (2007). ALOS PALSAR: A Pathfinder mission for Global-Scale Monitoring of the Environment. *IEEE Trans. Geosci. Remote Sensing* 45, 3307–3316. doi:10.1109/tgrs.2007.901027

Rosenqvist, A., Shimada, M., Suzuki, S., Ohgushi, F., Tadono, T., Watanabe, M., et al. (2014). Operational Performance of the ALOS Global Systematic Acquisition Strategy and Observation Plans for ALOS-2 PALSAR-2. *Remote Sensing Environ.* 155, 3–12. doi:10.1016/j.rse.2014.04.011

Saito, N., Yamada, H., and Yamaguchi, Y. (2018). "Study on Land Classification of PolSAR Data by Using Support Vector Machine," in 2018 IEEE International Workshop on Electromagnetics:Applications and Student Innovation Competition (iWEM). doi:10.1109/iWEM.2018.8536619

Sato, M., Chen, S. W., and Satake, M. (2012). Polarimetric SAR Analysis of Tsunami Damage Following the March 11, 2011 East Japan Earthquake. *Proc. IEEE* 100, 2861–2875. doi:10.1109/JPROC.2012.2200649

Scheuchl, B., Flett, D., Caves, R., and Cumming, I. (2014). Potential of RADARSAT-2 Data for Operational Sea Ice Monitoring. *Can. J. Remote Sensing* 30, 448–461. doi:10.5589/M04-011

Schuler, D., Lee, J. S., Kasilingam, D., and Pottier, E. (2004). Measurement of Ocean Surface Slopes and Wave Spectra Using Polarimetric SAR Image Data. *Remote Sensing Environ.* 91, 198–211. doi:10.1016/j.rse.2004.03.008

Schuler, D. L., Jansen, R. W., Lee, J. S., and Kasilingam, D. (2003). Polarisation Orientation Angle Measurements of Ocean Internal Waves and Current Fronts Using Polarimetric SAR. *IEE Proc. Radar Sonar Navig.* 150, 135. doi:10.1049/ip-rsn:20030492

Shafai, S. S., and Kumar, S. (2020). PolInSAR Coherence and Entropy-Based Hybrid Decomposition Model. *Earth Space Sci.* 7, e2020EA001279. doi:10.1029/2020EA001279

Singh, G., and Yamaguchi, Y. (2018). Model-Based Six-Component Scattering Matrix Power Decomposition. *IEEE Trans. Geosci. Remote Sensing* 56, 5687–5704. doi:10.1109/tgrs.2018.2824322

SNAP 8.0 released – STEP (2022). Available at: https://step.esa.int/main/snap-8-0-released/(Accessed January 3, 2022).

Stewart, C., Lasaponara, R., and Schiavon, G. (2013). ALOS PALSAR Analysis of the Archaeological Site of Pelusium. *Archaeol. Prospect.* 20, 109–116. doi:10.1002/ARP.1447

Thanh Noi, P., and Kappas, M. (2018). Comparison of Random Forest, K-Nearest Neighbor, and Support Vector Machine Classifiers for Land Cover Classification Using Sentinel-2 Imagery. *Sensors* 18, 18. doi:10.3390/s18010018

Tomar, K. S., Kumar, S., and Tolpekin, V. A. (2019). Evaluation of Hybrid Polarimetric Decomposition Techniques for Forest Biomass Estimation. *IEEE J. Sel. Top. Appl. Earth Observations Remote Sensing* 12, 3712–3718. doi:10.1109/jstars.2019.2947088

van Zyl, J. J. (1993). "Application of Cloude's Target Decomposition Theorem to Polarimetric Imaging Radar Data," in *Radar Polarimetry*. Editors H. Mott and W.-M. Boerner (San Diego: SPIE), 184–191. doi:10.1117/12.140615

Vapnik, V. N. (1995). "Introduction: Four Periods in the Research of the Learning Problem," in *The Nature of Statistical Learning Theory* (New York, NY: Springer New York), 1–14. doi:10.1007/978-1-4757-2440-0_1

Velotto, D., Migliaccio, M., Nunziata, F., and Lehner, S. (2011). Dual-polarized Terrasar-X Data for Oil-Spill Observation. *IEEE Trans. Geosci. Remote Sensing* 49, 4751–4762. doi:10.1109/tgrs.2011.2162960

Werninghaus, R., and Buckreuss, S. (2010). The TerraSAR-X mission and System Design. *IEEE Trans. Geosci. Remote Sensing* 48, 606–614. doi:10.1109/tgrs.2009.2031062

Yamaguchi, Y., Moriyama, T., Ishido, M., and Yamada, H. (2005). Four-component Scattering Model for Polarimetric SAR Image Decomposition. *IEEE Trans. Geosci. Remote Sensing* 43, 1699–1706. doi:10.1109/tgrs.2005.852084

Yamaguchi, Y., Yajima, Y., and Yamada, H. (2006). A Four-Component Decomposition of POLSAR Images Based on the Coherency Matrix. *IEEE Geosci. Remote Sensing Lett.* 3, 292–296. doi:10.1109/lgrs.2006.869986

Yin, Q., Cheng, J., Zhang, F., Zhou, Y., Shao, L., and Hong, W. (2020). Interpretable POLSAR Image Classification Based on Adaptive-Dimension Feature Space Decision Tree. *IEEE Access* 8, 173826–173837. doi:10.1109/access.2020.3023134

Yin, Q., Hong, W., Zhang, F., and Pottier, E. (2018). "Analysis of Polarimetric Feature Combination Based on Polsar Image Classification Performance with Machine Learning Approach," in IGARSS 2018-2018 IEEE International Geoscience and Remote Sensing Symposium. doi:10.1109/IGARSS.2018.8517585

Zhao, L., Zhang, Q., Li, Y., Qi, Y., Yuan, X., Liu, J., et al. (2021). China's Gaofen-3 Satellite System and its Application and Prospect. *IEEE J. Sel. Top. Appl. Earth Observations Remote Sensing* 14, 11019–11028. doi:10.1109/jstars.2021.3122304

Conflict of Interest: The authors declare that the research was conducted in the absence of any commercial or financial relationships that could be construed as a potential conflict of interest.

Publisher's Note: All claims expressed in this article are solely those of the authors and do not necessarily represent those of their affiliated organizations or those of the publisher, the editors, and the reviewers. Any product that may be evaluated in this article, or claim that may be made by its manufacturer, is not guaranteed or endorsed by the publisher.